

B ITP 2006/45
 hep-ph/0612182

Lightest sterile neutrino abundance within the M SM

Takehiko Asaka^a, Mikko Laine^b, Mikhail Shaposhnikov^a

^aInstitut de Theorie des Phenomenes Physiques, EPFL, CH-1015 Lausanne, Switzerland

^bFaculty of Physics, University of Bielefeld, D-33501 Bielefeld, Germany

Abstract

We determine the abundance of the lightest (dark matter) sterile neutrinos created in the Early Universe due to active-sterile neutrino transitions from the thermal plasma. Our starting point is the field-theoretic formula for the sterile neutrino production rate, derived in our previous work [JHEP 06 (2006) 053], which allows to systematically incorporate all relevant effects, and also to analyse various hadronic uncertainties. Our numerical results differ moderately from previous computations in the literature, and lead to an absolute upper bound on the mixing angles of the dark matter sterile neutrino. Comparing this bound with existing astrophysical X-ray constraints, we find that the Dodelson-Widrow scenario, which proposes sterile neutrinos generated by active-sterile neutrino transitions to be the sole source of dark matter, is only possible for sterile neutrino masses lighter than 3.5 keV (6 keV if all hadronic uncertainties are pushed in one direction and the most stringent X-ray bounds are relaxed by a factor of two). This upper bound may conflict with a lower bound from structure formation, but a definitive conclusion necessitates numerical simulations with the non-equilibrium momentum distribution function that we derive. If other production mechanisms are also operative, no upper bound on the sterile neutrino mass can be established.

1. Introduction

In recent works [1, 2] it has been demonstrated that an extension of the Minimal Standard Model (MSM) by three right-handed gauge-singlet fermions | sterile neutrinos | with masses smaller than the electroweak scale, allows to address a number of phenomena which cannot be explained in the framework of the MSM. Indeed there exists a parameter choice within this model, called the MSM in refs. [1, 2], which is consistent with experimentally observed neutrino masses and mixings, provides a candidate for dark matter particles, and can explain the baryon asymmetry of the Universe [2], through a CP-violating redistribution of the lepton number among active and sterile flavours [3], followed by an anomalous conversion of the lepton number in active flavours into a baryon number [4]. Adding to this model one neutral scalar field allows to accommodate inflation [5]. Moreover various astrophysical problems may find their explanations [6].

In the MSM, the role of dark matter is played by the lightest sterile neutrino, with a mass in the keV range. This dark matter candidate was proposed a while ago in ref. [7] from different considerations, and studied later on in a number of works [8]–[15]. It was pointed out in ref. [7] that the couplings of the dark matter sterile neutrino to charged leptons and active neutrinos can be so weak that it never equilibrates in the Early Universe. As has been stressed recently [16]–[21], this means that even if the exact values of the mixing angles between sterile and active neutrinos were known, the primordial abundance of the dark matter sterile neutrinos cannot be predicted. The reason is trivial: the kinetic equation describing sterile neutrino production is a first order differential equation in time, and in order to solve it one must specify the initial condition, on which the solution depends significantly, because inverse processes are much slower than the rate of Universe expansion. In more physical terms, one has to know the physics beyond the MSM to set the initial conditions; an example of a complete framework, involving the inflation, can be found in ref. [5].

Though a prediction of the primordial abundance of the dark matter sterile neutrinos requires physics beyond the MSM, an upper limit on the mixing angle between sterile and active neutrinos as a function of the sterile neutrino mass M_s ,

$$\sin^2(2\beta) < f(M_s); \quad (1.1)$$

can be established. Indeed, some number of sterile neutrinos are certainly produced in the Early Universe through the mixing with active neutrinos, and this amount must be smaller than the abundance of dark matter, known from observations. This upper bound can be derived with a small number of extra assumptions, which we formulate as follows:

- (i) The MSM is a good effective theory below energies of a few GeV, so that there are no interactions beyond those included in the MSM Lagrangian.
- (ii) The standard Big Bang scenario is valid starting from temperatures above a few GeV.

- (iii) The charge asymmetries of the plasma (particularly the asymmetries in the total lepton number, and in the various lepton flavours) are small, i.e. at most within a few orders of magnitude of the observed baryon asymmetry, at temperatures below a few GeV.
- (iv) The masses of the two heavier sterile neutrinos are large enough so that they decay above temperatures of a few GeV.

The assumptions (i-iii) are crucial. For example, if the atom is light, its interactions may result in sterile neutrino production at a low scale [5], making (i) invalid. For very low reheating temperatures after inflation, the assumption (ii) is not satisfied and the production of sterile neutrinos may be suppressed [22]. As for point (iii), it is known from ref. [8] that the rate of sterile neutrino production is in fact greatly boosted if relatively large lepton asymmetries (corresponding to chemical potentials $\approx T > 10^5$) are present. On the other hand, if the crucial assumptions (i-iii) are valid, the assumption (iv) can be relaxed: once the result is known, the decays of heavier sterile neutrinos can be taken into account *a posteriori* [19]. We will return to the last point below.

There are quite a number of computations of the function $f(M_s)$ already existing in the literature, starting from similar assumptions [7, 9, 10, 12, 13]. They are based, however, on kinetic equations which were not derived rigorously and which in fact differ from the expressions obtained from the first principles of statistical mechanics and quantum field theory [21]. Moreover, as discussed in ref. [21], neither the hadronic scattering contributions to the rate of sterile neutrino production, nor the uncertainties in the hadronic equation-of-state, have been exhaustively analyzed in refs. [7, 9, 10, 12, 13].

The aim of the present paper is therefore to apply the general formalism of ref. [21] to find the amount and spectrum of the sterile neutrinos created in active-sterile transitions. Our results differ from those that have previously appeared in the literature, even though it turns out that the order of magnitude remains the same.

Given the results of the theoretical computation, avoiding the overclosure of the Universe allows us to establish the constraint in Eq. (1.1). We can, however, also carry out a comparison with other astrophysical and cosmological limits on the properties of sterile neutrinos. Indeed, the sterile neutrino radiative decays $N \rightarrow \gamma \gamma$ produce a feature in the diffuse X-ray background [9, 16] or a line in the X-ray spectrum in the direction where dark matter is accumulated (such as clusters of galaxies [11, 18], dwarf galaxies [20], or galaxies [11, 20, 23, 24]). The position of this line, if found, determines the mass M_s of the sterile neutrino, while the line intensity would fix the mixing angle θ . No feature or line has been observed so far, which places a constraint on the mixing angle of the form $\sin^2(\theta) < f_X(M_s)$ [16, 18, 20, 23, 24, 25, 26, 27, 28, 29]. An exclusion plot from refs. [20, 26] is reproduced in Fig. 9 below, and can be compared with Eq. (1.1).

Another, completely independent constraint comes from cosmological structure formation, particularly in the form of Lyman- α forest observations [30]-[33]. Being relatively light, dark matter sterile neutrinos would play the role of warm dark matter, with a free-streaming

length exceeding greatly that of cold dark matter. This erases inhomogeneities on the smallest scales. An observation of the small scale structures puts, therefore, an upper bound on the free-streaming length and, consequently, on the average velocity of the dark matter particles. This converts to a lower bound on the inverse velocity, which can be expressed roughly as $M_s h_{\text{q}_a \text{ji}} = h_{\text{q}_s \text{ji}} > M_0$, where $h_{\text{q}_a \text{ji}}$ and $h_{\text{q}_s \text{ji}}$ are the average momenta of active and sterile neutrinos, respectively, at the moment of structure formation, and the value of M_0 is as large as $M_0 \approx 14.4$ keV according to ref. [32]. The computations of refs. [7, 10, 13] lead to a nearly-thermal spectrum of sterile neutrinos which is somewhat shifted in the infrared in comparison with the Fermi-Dirac distribution. According to ref. [13], $h_{\text{q}_s \text{ji}} = h_{\text{q}_a \text{ji}} \approx 0.9$ (uncertainties in this number and its dependence on the sterile neutrino mass will be discussed below). This leads to $M_s > 13$ keV [32], to again be compared with Eq. (1.1). Note that ref. [33] gives a somewhat weaker bound $M_s > 10$ keV. We stress that these mass bounds do depend on the mechanism of sterile neutrino production through the momentum distribution function of sterile neutrinos [19]. A model-independent constraint (the Tremaine-Gunn bound) on the mass coming from the analysis of the rotational curves of dwarf satellite galaxies [34, 35] is in fact much weaker and reads $M_s > 0.3$ keV [36].

These three different types of constraints, Eq. (1.1), X-ray, and Lyman-alpha or the Tremaine-Gunn bound, determine the allowed values for the mass and mixing angles of the dark matter sterile neutrino, necessary for planning for their search in space missions [29] and in laboratory experiments [37]. In addition, the validity of the Dodelson-Widrow scenario, where only thermal production is taken into account (so that Eq. (1.1) becomes an equality), can be tested.

The plan of the paper is the following. We start by reviewing the formalism of ref. [21] in Sec. 2. In Sec. 3 we apply it to the leptonic contribution to the sterile neutrino production rate, while in Sec. 4 the kinetic equation for the sterile neutrino abundance and its solution in the cosmological context are discussed. In Sec. 5 we analyse the hadronic contributions that play a role in the solution of the kinetic equation, and their uncertainties. In Sec. 6 we combine all these results together and present numerical estimates for the relic sterile neutrino abundance as a function of M_s and θ . In Sec. 7 we compare our results with the observational constraints mentioned above, and discuss the viability of the Dodelson-Widrow scenario for sterile neutrino production. We conclude in Sec. 8. In this paper the notations of ref. [21] will be used unless stated otherwise.

2. Review of the general formalism

As has been discussed in ref. [21], the assumptions (i-iv) allow to derive, from first principles, a general formula for the sterile neutrino production rate, provided that we choose parameter values consistent with the observational constraints mentioned above. The restriction to temperatures below a few GeV in these assumptions means that the electroweak symmetry

is broken, whereby it is an excellent approximation to replace the Higgs field by its vacuum expectation value $v' = 246$ GeV. Moreover combining the two sets of observational constraints restricts the mixing parameter(s) to be small. To be precise, there are several mixing parameters, θ_I , where I is the sterile neutrino flavour and θ is the active neutrino flavour. We define $\theta_I^2 = M_D^2 \theta_I^2 = M_I^2$, where M_D and M_I are the neutrino Yukawa couplings; and M_I are the sterile neutrino Majorana masses. In the following we choose the lightest sterile neutrino to correspond to $I = 1$. Because of the smallness of θ_I , $\theta_I^2 < 10^{-3}$ (or, in terms of Yukawa couplings, $|y_{11}|^2 < 10^{-11}$, $|y_{21}|^2, |y_{31}|^2 < 10^{-7}$), it is perfectly sufficient to restrict to leading order in a Taylor series in θ_I^2 , which simplification plays an essential role in the first-principles derivation presented in ref. [21]. (For $I = 2, 3$ these constraints derive from the baryon asymmetry of the Universe [2].) For future reference, let us also define

$$\theta_I^2 = \frac{\theta_I^2}{\theta_1^2} = e; \quad (2.1)$$

this angle corresponds to that in Eq. (1.1).

With these premises, the phase space density $n_I(t; q)$ of sterile neutrinos in either spin state,

$$n_I(t; q) = \sum_{s=1,2} \frac{dN_I^{(s)}(t; x; q)}{dx^3 dq^3}, \quad (2.2)$$

obeys the equation

$$\frac{\partial}{\partial t} H q \frac{\partial}{\partial q_i} n_I(t; q) = R(T; q); \quad (2.3)$$

where H is the Hubble parameter, $H = d \ln a(t)/dt$, and q_i are the spatial components of q . Note that in thermal equilibrium, $n_I(t; q) = 2n_F(q^0) = (2\pi)^3$, where n_F is the Fermi distribution function. The source term reads [21]

$$R(T; q) = \frac{4n_F(q^0)}{(2\pi)^3 2q^0} \frac{x^3}{\text{Tr} \not{q} \not{a}_L [2Q + \text{Re} \not{q}]^2} \frac{M_D \not{\theta}_I}{[\text{Im} \not{q}^2 + 4fQ + \text{Re} \not{q}] \text{Im} \not{q}} \quad (2.4)$$

$$= \frac{4n_F(q^0)}{(2\pi)^3 2q^0} \frac{x^3}{\not{q} \not{a}_L [2Q + \text{Re} \not{q}]^2} \frac{M_D \not{\theta}_I}{[\text{Im} \not{q}^2 + 4fQ + \text{Re} \not{q}]^2} \text{Im} \not{q} = a_R^0;$$

where Q is the on-shell four-momentum of the sterile neutrino (i.e. $Q^2 = M_I^2$); \not{q} is the self-energy of the active neutrino of flavour θ ; and a_L, a_R are the chiral projectors. It is obvious that $n_I(t; q)$ and $R(T; q)$ are functions of q only, and we will use the corresponding simplified notation in the following.

Now, the real part $\text{Re} \not{q}$ of the active neutrino self-energy is generated at 1-loop level through W and Z -boson exchange. At low energies, the result can be expanded in $1 = m_W^2$, $1 = m_Z^2$. In the absence of leptonic chiral potentials, the first term in the expansion vanishes, and the leading contribution comes from the second term. Writing the result as

$$\text{Re} \not{q} = \not{q} a_L(Q) + \not{q} b(Q); \quad (2.5)$$

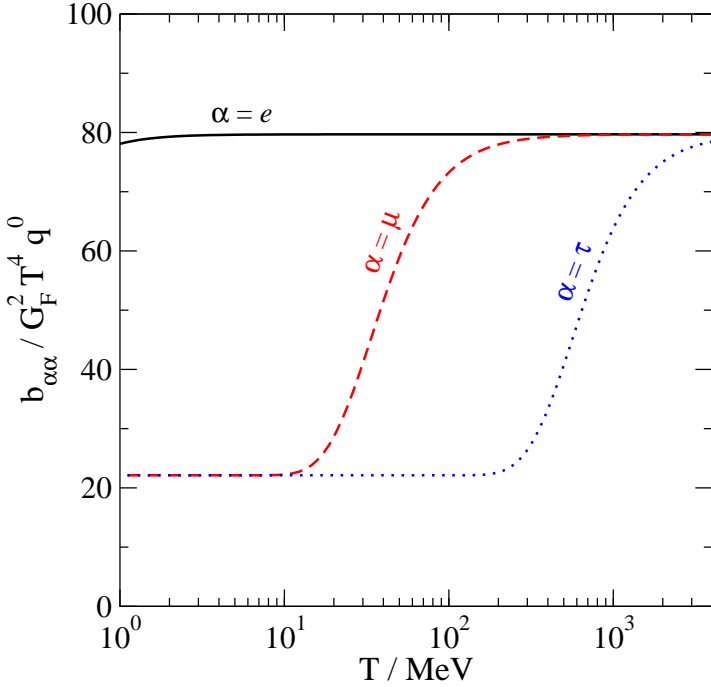


Figure 1: The function $b_\alpha(Q)$ that determines the real part $\text{Re } \mathcal{G}(Q)$ (cf. Eq. (2.5)), in units of $G_F^2 T^4 q^0$, as a function of the temperature T and the active neutrino flavour, with $\alpha = e; \mu; \tau$. We have assumed here that $\mathbf{p}_1^0 \neq m_w$.

where $u = (1; 0)$, we note that the function $a_\alpha(Q)$ can be ignored, since it is small compared with the tree-level term \mathcal{G} . On the other hand the latter structure in Eq. (2.5) does not appear at tree-level, and needs to be kept. For $q = m_w$ it reads [38, 39]

$$b_\alpha(Q) = \frac{16G_F^2}{m_w} q^0 \frac{h}{2} (m_1) + \cos^2 \frac{i}{m_w} (m) ; \quad (2.6)$$

where $G_F = g_w^2 = 4 \frac{p}{2m_w^2}$ is the Fermi constant, m_1 is the mass of the charged lepton of generation $(l_1 = e; \mu; \tau)$, and $m = 0$ is the mass of the SM active neutrino. The function h is finite and easily evaluated numerically:

$$h(m) = \frac{1}{(2\pi)^3} \frac{d^3 p}{2E} \frac{4}{3} \frac{p^2}{p^2 + m^2} : \quad (2.7)$$

Note, in particular, that $h(0) = 7^2 T^4 = 360$. The functions b_α are plotted in Fig. 1.

As concerns the imaginary part $\text{Im } \mathcal{G}$, there is a 1-loop contribution from the same graphs as for $\text{Re } \mathcal{G}$, but it is exponentially suppressed, $\exp(-m_w/T)$ (cf. Sec. 3.1). Therefore, at low temperatures, the dominant contribution is generated by those 2-loop graphs which are not exponentially suppressed. The dependence on Q is more complicated than in Eq. (2.6): in general $\text{Im } \mathcal{G}(Q) = G_F^2 T^5 f(Q; T)$, where f is a non-trivial dimensionless function, which is numerically of order unity.

Given that $\text{Im } \text{Re}$ because of the w -suppression, and that $\text{Re } \text{ub} (Q)$ because of the reasons mentioned above, the expression in Eq. (2.4) can be simplified. Carrying out the Dirac traces; combining equivalent terms; and re-introducing Dirac traces and chiral projectors $a_L; a_R$ around $\text{Im} = 0$ at the end, as a reminder of our convention of showing them explicitly [21], we arrive at

$$R(T; q) = \frac{\frac{4n_F(q^0)}{(2\pi)^3 2q^0} x^3}{\frac{M_1^2 + b^2}{M_1^2 + 2q^0 b + b^2}} \frac{\text{Tr } \not{M}_D \not{f}_I}{\text{Tr } \not{a}_L \text{Im} = a_R + 2(M_1^2 + q^0 b) b \text{Tr } \not{a}_L \text{Im} = a_R}; \quad (2.8)$$

where $b = b(Q)$, and we made use of $Q^2 = M_1^2$.

Now, let us estimate the orders of magnitude that are relevant for Eq. (2.8) (for analogous earlier discussions see, e.g., refs. [7, 9]). We consider momenta of order $q \ll T$, where the rate turns out to peak; temperatures in the range $1 \text{ MeV} \leq T \leq 10 \text{ GeV}$; and sterile neutrino masses in the range $10^{-1} \text{ keV} \leq M_1 \leq 10^3 \text{ keV}$. Thereby $q^0 \ll T \ll M_1$, and $b \ll 50G_F^2 T^5$ (cf. Fig. 1). We now identify two different temperature scales:

We define T_1 such that $M_1^2 = 2q^0 b$ for $T = T_1$, i.e.

$$T_1 = \frac{M_1}{10G_F} \frac{1}{3} \quad 200 \text{ MeV} \quad \frac{M_1}{\text{keV}} \frac{1}{3} : \quad (2.9)$$

Note that for $T = T_1$, $b^2 = M_1^2$, and obviously also $b = q^0$.

We define T_2 such that $M_1^2 = b^2$ for $T = T_2$, i.e.

$$T_2 = \frac{M_1}{50G_F^2} \frac{1}{5} \quad 2.7 \text{ GeV} \quad \frac{M_1}{\text{keV}} \frac{1}{5} : \quad (2.10)$$

Note that for $T = T_2$, $q^0 b = M_1^2$, while it is still true that $b = q^0$.

Let us then estimate the magnitude of the second row in Eq. (2.8) for various temperatures. For simplicity we set $\text{Im} = G_F^2 T^5$, since the precise magnitude plays no role, given that Im appears linearly in all terms in the numerator. We observe that:

For $T = T_1$, M_1^2 dominates in magnitude over all thermally generated terms. The second row of Eq. (2.8) then evaluates to $G_F^2 T^6 = M_1^2$, i.e. decreases fast at low T .

For $T = T_2$, the second row evaluates to $1 = 10^5$. This is the peak value.

For $T = T_2$, the denominator is dominated by $(2q^0 b)^2$ and thus starts to increase. The second row of Eq. (2.8) then evaluates to $M_1^2 = 10^4 G_F^2 T^6$, i.e. decreases again fast.

Once $T = T_2$, the two terms in the numerator of Eq. (2.8) are of the same order of magnitude. In fact, the first term becomes negative, but this effect is compensated for by the second term, so that the expression as a whole remains positive. The overall magnitude is now $G_F^2 T_2^4$, i.e. about 1=10⁶ of that at $T = T_1$.

For $T = T_2$, the second row increases as $G_F^2 T^4$. Given that $G_F = (290 \text{ GeV})^2$, however, these contributions remain very small in the region $T < 10 \text{ GeV}$. Moreover in practice our rough approximation turns out to be an overestimate, when compared with the exact numerical evaluation.

To confirm this qualitative picture, we have verified numerically that if one starts the integration (to be specified in Sec. 4) from a high temperature $T = 10 \text{ GeV} = T_2$, then both terms in the numerator of Eq. (2.8) need to be taken into account, in order to obtain a positive production rate (in the range $T > (5::10) \text{ GeV}$ the exponentially suppressed 1-loop contribution to Im needs to be taken account as well, but this does not change the conclusions). Their combined contribution from the high-temperature region is, however, completely negligible. For the dark matter sterile neutrino it is therefore in practice enough to start the integration from $T = T_2$ a few GeV, and keep only the first term in the numerator, which is what we will do in the following.

3. Leptonic contribution to the production rate

3.1. 1-loop effects

We now proceed to determine Im . We assume that the temperature is well below the temperature T_{ew} where the electroweak crossover takes place, $T_{\text{ew}} = 100 - 200 \text{ GeV}$. In this situation the Higgs phenomenon provides for a good tool for carrying out perturbative computations. The simplest contributions to Im come from the same 1-loop graphs as were considered for Re , involving a single W or Z^0 propagator; however we do not carry out any expansion in the inverse W or Z^0 masses like for Re . A straightforward computation in Feynman gauge yields

$$\begin{aligned} \text{Im}_{\text{lep}}^{1\text{-loop}}(Q) = & \frac{w n_F^{-1}(q^0)}{p_C} \int_{C=W, Z}^X \frac{d^3 p_1}{(2\pi)^3 2E_1} \int_{C=W, Z}^Z \frac{d^3 p_2}{(2\pi)^3 2E_2} \text{Re} \left[\right. \\ & \left. (2\pi)^4 \text{Im}^{(4)}(P_1 + P_2 - Q) n_{F1} n_{B2} + \text{diagram 1} \right. \\ & + (2\pi)^4 \text{Im}^{(4)}(P_2 - P_1 - Q) n_{B2} (1 - n_{F1}) + \text{diagram 2} \\ & + (2\pi)^4 \text{Im}^{(4)}(P_1 - P_2 - Q) n_{F1} (1 + n_{B2}) + \text{diagram 3} \\ & + (2\pi)^4 \text{Im}^{(4)}(P_1 + P_2 + Q) (1 - n_{F1}) (1 + n_{B2}) ; \text{diagram 4} \end{aligned} \quad (3.1)$$

where $n_{F_i} = n_F(E_i)$, $n_{B_i} = n_B(E_i)$; and $p_W = 2, p_Z = \cos^2 \theta_W$ are the "weights" of the charged and neutral current channels. Furthermore, $P_i = (E_i; p_i)$ are on-shell four-momenta,

$$E_1 = \frac{q}{p_1^2 + m_k^2}; \quad E_2 = \frac{q}{p_2^2 + m_c^2}; \quad (3.2)$$

where $m_k = m_1$ and $m_c = m_2 = 0$. The graphs in Eq. (3.3) illustrate the various processes, with the wavy line indicating the weak gauge boson. The phase space integrals remaining can be evaluated numerically as explained in Appendix A.

For the masses that we are interested in, m_1, m_2, m_W , only one of the channels in Eq. (3.1) gives a non-zero contribution, namely the second one.

Now, as discussed in the previous section, the dominant production of N_1 takes place at temperatures much below m_W , say, $T < m_W = 10$. In this case the phase space factor n_{B2} guarantees that the 1-loop contribution is suppressed by at least $\exp(-m_W/T)$, and thus vanishingly small. One might worry that thermal effects on the W boson mass make $m_W(T)$ smaller than naively expected; at the very small temperatures we are interested in, however, this effect is negligible. Therefore, the 1-loop contribution is indeed inessential for our purposes, and does not play a role in the following.

3.2. 2-loop effects

We now move to specifying the 2-loop contribution to Im in Eq. (2.8), originating from intermediate states containing leptons only. These effects can be reliably treated within perturbation theory, and are not exponentially suppressed at low temperatures. At the same time, previous evaluations in the literature have made use of phenomenological approximations which are not part of the strict perturbative computation, particularly in order to simplify the Dirac structures that enter the sterile neutrino production rate. In the following we evaluate the leptonic contributions without any such approximations.

In order to proceed, it is actually helpful to start by recalling the contribution that emerges from a pair of free quarks, with masses m_2, m_3 ; the derivation of this result has been discussed in explicit detail in ref. [21]. The final result, given by Eq. (3.41) of ref. [21], reads:

$$\begin{aligned} \text{Im}_{\text{had}}^{2\text{-loop}}(Q) = & 2N_c G_F^2 n_F^{-1}(q^0) \sum_{C=W,Z} \frac{X}{p_C} \frac{Z}{(2\pi)^3 2E_1} \frac{d^3 p_1}{(2\pi)^3 2E_2} \frac{Z}{(2\pi)^3 2E_3} \frac{d^3 p_2}{(2\pi)^3 2E_3} \\ & (2\pi)^4 \stackrel{(4)}{(P_1 + P_2 + P_3 - Q) n_{F1} n_{F2} n_{F3} A(m_k; m_2; m_3)} + \text{Diagram 1} \\ & + (2\pi)^4 \stackrel{(4)}{(P_2 + P_3 - P_1 - Q) n_{F2} n_{F3} (1 - n_{F1}) A(m_k; m_2; m_3)} + \text{Diagram 2} \\ & + (2\pi)^4 \stackrel{(4)}{(P_1 + P_3 - P_2 - Q) n_{F1} n_{F3} (1 - n_{F2}) A(m_k; m_2; m_3)} + \text{Diagram 3} \\ & + (2\pi)^4 \stackrel{(4)}{(P_1 + P_2 - P_3 - Q) n_{F1} n_{F2} (1 - n_{F3}) A(m_k; m_2; m_3)} + \text{Diagram 4} \\ & + (2\pi)^4 \stackrel{(4)}{(P_1 - P_2 - P_3 - Q) n_{F1} (1 - n_{F2}) (1 - n_{F3}) A(m_k; m_2; m_3)} + \text{Diagram 5} \end{aligned}$$

$$\begin{aligned}
& + (2)^4 (4) (P_2 \cdot P_1 \cdot P_3 \cdot Q) n_{F2} (1 - n_{F1}) (1 - n_{F3}) A(m_k; m_2; m_3) + \text{graph 1} \\
& + (2)^4 (4) (P_3 \cdot P_1 \cdot P_2 \cdot Q) n_{F3} (1 - n_{F1}) (1 - n_{F2}) A(m_k; m_2; m_3) + \text{graph 2} \\
& + (2)^4 (4) (P_1 \cdot P_2 \cdot P_3 \cdot Q) (1 - p_1) (1 - p_2) (1 - p_3) A(m_k; m_2; m_3) + \text{graph 3}
\end{aligned} \tag{3.3}$$

where $n_{Fi} = n_F(E_i)$;

$$A(m_k; m_2; m_3) = \frac{h}{(p_1 + m_k)} \text{Tr} \frac{h}{(p_2 + m_2)} \frac{h}{(p_3 + m_3)} ; \tag{3.4}$$

p_2, p_3 are the "weights" of the charged and neutral current channels; and m_k has the same meaning as in Eq. (3.2). Furthermore, $P_i(E_i; p_i)$ are again on-shell four-momenta, now with the mass assignments

$$E_1 = \frac{q}{p_1^2 + m_k^2}; \quad E_2 = \frac{q}{p_2^2 + m_2^2}; \quad E_3 = \frac{q}{p_3^2 + m_3^2}; \tag{3.5}$$

The graphs in Eq. (3.3) illustrate the various processes. Further details (in particular the values of the masses $m_2; m_3$ and of the Dirac matrix) will be explained presently.

Considering then the leptonic contributions, it is obvious that the same eight kinematic possibilities will appear as in Eq. (3.3), just with different masses and coefficients. On the other hand additional terms appear as well, since Z -exchange can proceed through more channels than in the hadronic case.

Given that the kinematic possibilities are identical, however, it is possible to "factorise" the result into a "Dirac part" and a "kinematic part". It is therefore enough to show the result for the Dirac part by considering one of the kinematic channels only; for simplicity we choose the alternative in Eq. (3.3) where all masses are positive inside the A -function. A straightforward computation parallelling the one in ref. [21] then produces the result

$$\begin{aligned}
\text{Im}_{\text{loop}}^{\text{2-loop}}(Q) = & 2G_F^2 n_F^{-1}(q^0) \frac{Z}{(2)^3 2E_1} \frac{d^3 p_1}{(2)^3 2E_2} \frac{Z}{(2)^3 2E_3} \frac{d^3 p_2}{(2)^3 2E_3} \frac{Z}{(2)^3 2E_1} \frac{d^3 p_3}{(2)^3 2E_1} \\
& \times \text{Tr} \frac{h}{(p_1 + m_1)} \frac{h}{(p_2 + m_1)} \frac{h}{(p_3 + m_1)} a_L \frac{h}{(p_3 + m_1)} a_L + \\
& 2(p_1 + m_1) = e; \\
& + \frac{1}{2} (p_1 + m_1) = e; \\
& + \frac{3}{4} (p_1 + m_1) = e; \\
& \frac{3}{4} (p_1 + m_1) a_L (p_2 + m_1) a_L (p_3 + m_1) \\
& (p_1 + m_1) (p_2 + m_1) a_L (p_3 + m_1)
\end{aligned}$$

$$\begin{aligned}
& (\not{p}_1 + m_1) a_L (\not{p}_2 + m_1) (\not{p}_3 + m_1) \\
& (2)^4 (4) (\not{p}_2 - \not{p}_1 - \not{p}_3 - Q) n_{F2} (1 - n_{F1}) (1 - n_{F3}) + \dots ; \text{Diagram} \quad (3.6)
\end{aligned}$$

where now $1=2+2x_w + 5=2$, with $x_w = \sin^2 \theta_w$, and the energies E_i are on-shell with the obvious mass assignments.

Inspecting Eqs. (2.8) and (3.6), we observe that two kinds of Dirac traces appear in the final result: either a product of two traces, or a single trace. Both cases are elementary, and result in

$$\begin{aligned}
T_1 & \stackrel{h}{\text{Tr}} \not{E} a_L (\not{p}_1 + m_1) \stackrel{i}{a_R} \text{Tr} (\not{p}_2 + m_2) (a + b_5) (\not{p}_3 + m_3) (a + b_5) \\
& = 16 \stackrel{h}{(a - b)^2} \not{p}_1 \not{p}_3 E + (a + b) \not{p}_1 \not{p}_2 E + (b - a) m_2 m_3 \not{p}_1 E; \quad (3.7) \\
T_2 & \stackrel{h}{\text{Tr}} \not{E} a_L (\not{p}_1 + m_1) (a + b_5) (\not{p}_2 + m_2) (c + d_5) (\not{p}_3 + m_3) \stackrel{i}{a_R} \\
& = 8 \stackrel{h}{2(a + b)(c + d)} \not{p}_1 \not{p}_2 E + (a + b)(c - d) \not{p}_1 \not{p}_3 E + \\
& + (a - b)(c - d) \not{p}_1 \not{p}_2 E + (a - b)(c + d) \not{p}_2 \not{p}_3 E; \quad (3.8)
\end{aligned}$$

where the "external" four-vector E is either Q or u (cf. Eq. (2.8)).

Given these ingredients | the kinematic channels in Eq. (3.3), the Dirac structures in Eq. (3.6), and the traces in Eqs. (3.7), (3.8) | we can finally collect together the full expression needed in Eq. (2.8). We obtain

$$\begin{aligned}
\text{Tr} \not{E} a_L \not{m} & = (Q) a_R = 2G_F^2 n_F^{-1} (q^0) \stackrel{i}{\text{X}} \stackrel{Z}{C_i} \frac{d^3 p_1}{(2)^3 2E_1} \frac{Z}{(2)^3 2E_2} \frac{Z}{(2)^3 2E_3} \\
& + (2)^4 (4) (\not{p}_1 + \not{p}_2 + \not{p}_3 - Q) n_{F1} n_{F2} n_{F3} T_i(m_1; m_2; m_3) + \text{Diagram} \\
& + (2)^4 (4) (\not{p}_2 + \not{p}_3 - \not{p}_1 - Q) n_{F2} n_{F3} (1 - n_{F1}) T_i(m_1; m_2; m_3) + \text{Diagram} \\
& + (2)^4 (4) (\not{p}_1 + \not{p}_3 - \not{p}_2 - Q) n_{F1} n_{F3} (1 - n_{F2}) T_i(m_1; m_2; m_3) + \text{Diagram} \\
& + (2)^4 (4) (\not{p}_1 + \not{p}_2 - \not{p}_3 - Q) n_{F1} n_{F2} (1 - n_{F3}) T_i(m_1; m_2; m_3) + \text{Diagram} \\
& + (2)^4 (4) (\not{p}_1 - \not{p}_2 - \not{p}_3 - Q) n_{F1} (1 - n_{F2}) (1 - n_{F3}) T_i(m_1; m_2; m_3) + \text{Diagram} \\
& + (2)^4 (4) (\not{p}_2 - \not{p}_1 - \not{p}_3 - Q) n_{F2} (1 - n_{F1}) (1 - n_{F3}) T_i(m_1; m_2; m_3) + \text{Diagram} \\
& + (2)^4 (4) (\not{p}_3 - \not{p}_1 - \not{p}_2 - Q) n_{F3} (1 - n_{F1}) (1 - n_{F2}) T_i(m_1; m_2; m_3) + \text{Diagram} \\
& + (2)^4 (4) (-\not{p}_1 - \not{p}_2 - \not{p}_3 - Q) (1 - n_{F1}) (1 - n_{F2}) (1 - n_{F3}) T_i(m_1; m_2; m_3); \text{Diagram} \quad (3.9)
\end{aligned}$$

where T_i equals T_1 or T_2 , as specified in Table 1. The prefactors C_i and the masses m_1, m_2, m_3 relevant for each channel are also listed in Table 1. For completeness and future reference, we have included in this Table the perturbative hadronic contributions as well.

4. Solution of the kinetic equation

Now that the ingredients entering Eq. (2.3) are in place, we need to discuss the solution of this equation, and identify the precise information about the equation-of-state which is needed for the solution. The considerations that follow are rather standard (see, e.g., refs. [7, 9]), but we present them here for completeness and in order to fix the notation.

It is convenient to represent the rate $R(T; q)$ as a function F of dimensionless variables,

$$R(T; q) = G_F^2 T^5 F \frac{m_i}{T} \frac{q}{T} ; \quad (4.1)$$

where m_i are the masses of the particles of the SM and of the sterile neutrinos. We also introduce the effective numbers of massless bosonic degrees of freedom $g_e(T)$ and $h_e(T)$ via the relations

$$e(T) = \frac{2T^4}{30} g_e(T) ; \quad s(T) = \frac{2^2 T^3}{45} h_e(T) ; \quad (4.2)$$

where $e(T)$ and $s(T)$ are the energy and entropy densities, respectively. Given the equation-of-state of the plasma [i.e. the relation between the pressure and the temperature, $p = p(T)$], $g_e(T)$ and $h_e(T)$ can be found from the standard thermodynamical relations

$$g_e(T) = \frac{30}{2T^2} \frac{d}{dT} \frac{p}{T} ; \quad h_e(T) = \frac{45}{2^2 T^3} \frac{dp}{dT} ; \quad (4.3)$$

Furthermore the sound speed squared, $c_s^2(T) = p^0(T) = e^0(T) = p^0(T) = T p^0(T)$, can be expressed as

$$\frac{1}{c_s^2(T)} = 3 + \frac{T h_e^0(T)}{h_e(T)} ; \quad (4.4)$$

where a prime denotes a derivative with respect to T . The Hubble rate is given by

$$H = \frac{T^2}{M_0(T)} ; \quad M_0(T) = M_{Pl} \frac{45}{4^3 g_e(T)} ; \quad (4.5)$$

where M_{Pl} is the Planck mass. Note that, from the assumption (iv) in Sec. 1, the heavier sterile neutrinos do not contribute to g_e and h_e for the temperatures of interest. Furthermore, the contributions from the lightest sterile neutrino are negligibly small as long as it does not get thermalized.

The kinetic equation (2.3) can easily be integrated by writing $n_I(t; q) = f(t; y)$, where the variable $y = a(t)q$ accounts for red-shift. After simple manipulations one gets the distribution function of sterile neutrinos at temperature T_0 :

$$n_I(t_0; q) = \frac{G_F^2}{3} \int_{T_0}^{T_1} dT \frac{M_0(T) T^2}{c_s^2(T)} F \frac{m_i}{T} ; \frac{q}{T_0} \frac{h_e(T)}{h_e(T_0)}^{\frac{1}{3}} ; \quad (4.6)$$

channel	C_i	T_i	m_1	m_2	m_3	a	b	c	d
WW + hadrons	$2N_c \mathcal{Y}_{ud} \frac{f}{f}$	T_1	m_1	m_d	m_u	$+\frac{1}{2}$	$\frac{1}{2}$		
	$2N_c \mathcal{Y}_{us} \frac{f}{f}$	T_1	m_1	m_s	m_u	$+\frac{1}{2}$	$\frac{1}{2}$		
	$2N_c \mathcal{Y}_{cd} \frac{f}{f}$	T_1	m_1	m_d	m_c	$+\frac{1}{2}$	$\frac{1}{2}$		
	$2N_c \mathcal{Y}_{cs} \frac{f}{f}$	T_1	m_1	m_s	m_c	$+\frac{1}{2}$	$\frac{1}{2}$		
ZZ + hadrons	$N_c=2$	T_1	0	m_u	m_u	$+\frac{1}{2}$	$\frac{4}{3} x_w$	$\frac{1}{2}$	
	$N_c=2$	T_1	0	m_c	m_c	$+\frac{1}{2}$	$\frac{4}{3} x_w$	$\frac{1}{2}$	
	$N_c=2$	T_1	0	m_d	m_d	$\frac{1}{2} + \frac{2}{3} x_w$	$+\frac{1}{2}$		
	$N_c=2$	T_1	0	m_s	m_s	$\frac{1}{2} + \frac{2}{3} x_w$	$+\frac{1}{2}$		
WW + leptons	2	T_1	m_1	m_e	0	$+\frac{1}{2}$	$\frac{1}{2}$		
	2	T_1	m_1	m	0	$+\frac{1}{2}$	$\frac{1}{2}$		
	2	T_1	m_1	m	0	$+\frac{1}{2}$	$\frac{1}{2}$		
	1=2	T_1	0	m_e	m_e	$\frac{1}{2} + 2x_w$	$+\frac{1}{2}$		
ZZ + leptons	1=2	T_1	0	m	m	$\frac{1}{2} + 2x_w$	$+\frac{1}{2}$		
	1=2	T_1	0	m	m	$\frac{1}{2} + 2x_w$	$+\frac{1}{2}$		
	1=2	T_1	0	0	0	$\frac{1}{2} + 2x_w$	$+\frac{1}{2}$		
	9=4	T_1	0	0	0	$+\frac{1}{2}$	$\frac{1}{2}$		
WZ + leptons	3=4	T_2	0	0	0	$+\frac{1}{2}$	$\frac{1}{2}$	$+\frac{1}{2}$	$\frac{1}{2}$
	1	T_2	m_1	m_1	0	$\frac{1}{2} + 2x_w$	$+\frac{1}{2}$	$+\frac{1}{2}$	$\frac{1}{2}$
	1	T_2	0	m_1	m_1	$+\frac{1}{2}$	$\frac{1}{2}$	$\frac{1}{2} + 2x_w$	$+\frac{1}{2}$

Table 1: The coefficients and masses that appear in Eq. (3.9), in the perturbative limit. The functions T_1 and T_2 , which depend on the masses m_1, m_2, m_3 and the coefficients a, b, c, d (which take values as specified above), are defined in Eqs. (3.7) and (3.8), respectively. The symbols 1 stand for leptons of generation , i.e. $m_1 = m_e; m_2 = m; m_3 = m$.

The integral of Eq. (4.6) over the momenta q gives the number density of sterile neutrinos, which can conveniently be normalized with respect to its would-be equilibrium value, $n_{\text{eq}}(t_0) = 3/(3T_0^3)^{1/2}$:

$$\frac{n_I(t_0)}{n_{\text{eq}}(t_0)} = \frac{8G_F^2}{9(3)} \int_{T_0}^{Z_1} dT \int_0^{Z_1} dz z^2 \frac{M_0(T)T^2}{c_s^2(T)h_e(T)} F \frac{m_i}{T}; z \quad : \quad (4.7)$$

Finally another characterization of the same quantity is obtained by normalizing through the total entropy density, which produces the so-called yield parameter:

$$Y_I(t_0) = \frac{n_I(t_0)}{s(t_0)} = \frac{30G_F^2}{9(3)} \int_{T_0}^{Z_1} dT \int_0^{Z_1} dz z^2 \frac{M_0(T)T^2}{c_s^2(T)h_e(T)} F \frac{m_i}{T}; z \quad : \quad (4.8)$$

The benefit of Eq. (4.8) is that it obtains, unlike Eq. (4.7), a constant value at low temperatures (in the absence of entropy production), because the factor $h_e(T_0)$ drops out.

To summarize, to find the relic concentration of sterile neutrinos produced by active-sterile transitions, one should have a reasonable approximation for the hadronic equation-of-state $p(T)$ and for its first and second temperature derivatives, $p'(T)$ and $p''(T)$.

To convert the result of Eq. (4.8) to physical units, we denote the contribution to the number density of the lightest sterile neutrino ($I = 1$) from an active neutrino of flavour e by n_1 (so that $n_1 = \frac{P}{s} = e; n_1$). To relate this quantity to s , we write

$$_1 \frac{M_1 n_1}{c_r} = \frac{M_1 Y_1}{c_r s}; \quad (4.9)$$

where $Y_1 = n_1/s$. From Particle Data Group [51], one finds $c_r = 1.054 \cdot 10^5 \text{ h}^2 \text{ GeV cm}^{-3}$ and $s = 7.04 n = 2886 \text{ cm}^{-3}$; yielding $c_r/s = 3.65 \cdot 10^9 \text{ h}^2 \text{ GeV}$. Then the result of Eq. (4.8) can be expressed as

$$_1 \text{h}^2 = 0.11 C(M_1) \frac{M_D j_1}{0.1 \text{ eV}}^2; \quad (4.10)$$

where $C(M_1) = 2.49 \cdot 10^5 \quad Y_1 = \frac{2}{1} \quad (\text{keV} \Rightarrow M_1)$.

The total relic density of the lightest sterile neutrino is now given by $\frac{P}{s} = e; \quad _1 \text{h}^2$. On the other hand, the dark matter density in the present Universe has been precisely measured by the WMAP collaboration [40] (68% CL):

$$_{\text{dm}} \text{h}^2 = 0.105^{+0.007}_{-0.013}; \quad (4.11)$$

Therefore, to avoid the overclosure of the Universe by N_1 , we get $\frac{P}{s} = e; \quad _1 \text{h}^2 < 0.112$, which leads to

$$\frac{X}{s} C(M_1) \frac{M_D j_1}{0.1 \text{ eV}}^2 < 1.0; \quad (4.12)$$

This corresponds to Eq. (1.1). In the following, we will present our results for the functions $C(M_1)$ defined by Eq. (4.10).

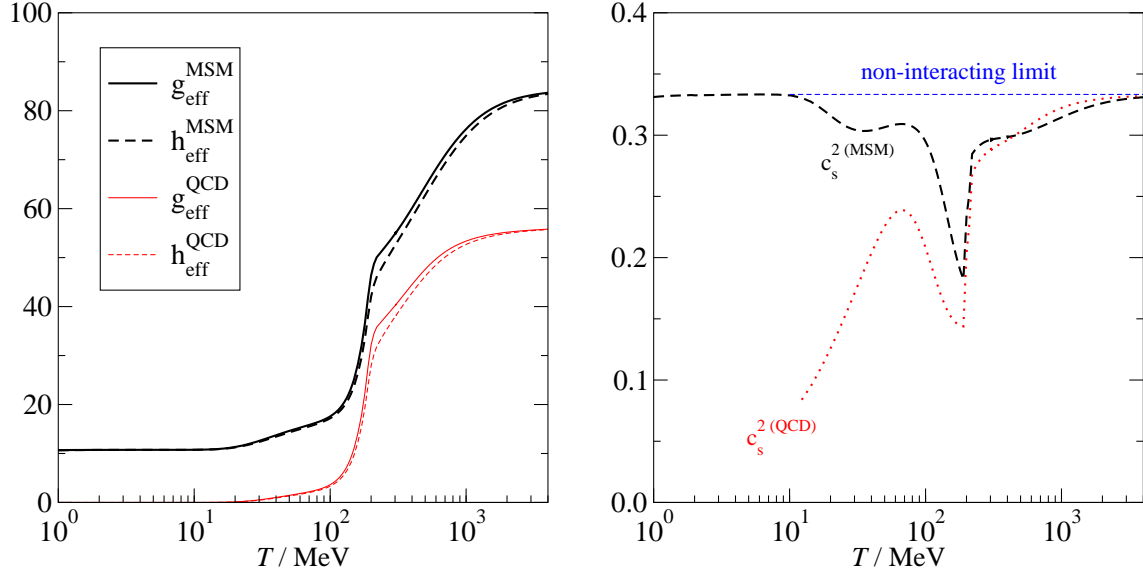


Figure 2: Left: g_{eff} ; h_{eff} as defined in Eq. 4.3), for the M SM and for the QCD part thereof, for $T = 1 \text{ MeV} \dots 4 \text{ GeV}$ (for more details, see ref. [43]). Right: the speed of sound squared c_s^2 , for the same system s. Various sources of uncertainties in these estimates are discussed in the text.

5. Hadronic uncertainties

As discussed in ref. [21], there are in principle three sources of hadronic effects and corresponding hadronic uncertainties in the present computation: those entering Re , Im , as well as the overall equation-of-state through the considerations in Sec. 4. The hadronic contributions to Re are suppressed by w with respect to the leptonic ones and will be omitted in the following. The hadronic contributions to Im arise at the same order as the leptonic ones, constituting thus a significant source term. Even more important are the hadronic contributions to the equation-of-state, since in the temperature range of interest hadrons completely dominate over leptons as far as the change in the effective number of light degrees of freedom is concerned (cf. Fig. 2). On the other hand, the hadronic effects in the equation-of-state are understood somewhat better than the ones in Im , given that they are theoretically more straightforward to access, both in the framework of the weak-coupling expansion [41]–[43] and of lattice simulations [44]–[47], so that the relative uncertainties are perhaps smaller than in Im . In fact we estimate the absolute uncertainties from these two sources to be of similar magnitudes. In the following we discuss the ways in which we extract these two quantities and try to estimate their uncertainties.

5.1. QCD equation-of-state

A basic fact to realise about the QCD equation-of-state is that the low-temperature hadronic world and the high-temperature partonic world can be analytically connected to each other, by tuning quark masses and the temperature: at non-zero quark masses there is no order parameter to distinguish between the two situations. Moreover, lattice simulations have been suggesting for quite a while already that such an analytical "crossover" is met even if the quark masses are not tuned but kept at their physical values; for a recent studies see, e.g., refs. [48]. In fact, these statements could even have been made without recourse to lattice simulations: the thermodynamics of a dilute "gas" of hadronic resonances at low temperatures, and of interacting quarks and gluons at high temperatures, appear to extrapolate to each other surprisingly well, when determined precisely enough [43].

Now, even if there only were a smooth crossover in the system, it is conventional to assign a (pseudo)critical temperature to it; we will denote this temperature by T_c . Of course T_c cannot be determined precisely, but the "conceptual" ambiguities involved do not appear to be much larger than the current statistical uncertainties. A recent large-scale lattice study, for instance, suggests that $T_c \approx 192 - 8 \text{ MeV}$ [49].

On the other hand, it is also important to realise that at the current moment the lattice studies still involve systematic uncertainties (related for instance to finite-volume effects or the absence of a precise continuum extrapolation), which are not quantitatively under control. Consequently, even though the final word on the value of T_c and on what happens around it lies with the lattice simulations, they are still rather far from establishing the correct behaviour in a wide temperature interval. In fact, even the results of various groups employing similar techniques differ by much more than the statistical uncertainties cited above [50]. Moreover, lattice studies fail to show any signs of the characteristic peak that physical pions cause in the sound speed at $T \approx 70 \text{ MeV}$ [43] (see also Fig. 2), a problem which can probably be assigned to the fact that the quark discretizations used in the current finite-temperature simulations do not respect the chiral symmetry that plays an essential role at low temperatures, and also tend to employ unphysically heavy quark masses. Lattice simulations also cannot be applied at very high temperatures. To summarise, the current numbers can be expected to be fairly reliable in the range from about T_c to about $(2-3)T_c$ at best.

For these reasons, we prefer to adhere to the procedure introduced in ref. [43] here, rather than to lattice simulations. It makes use of a gas of hadronic resonances at low temperatures; the most advanced (up to resummed 4-loop level [41]) weak-coupling results at high temperatures; and an interpolation thereof at intermediate temperatures.¹ Remarkably, the temperature interval where an interpolating function is needed in order to sew together the two asymptotic functions is fairly narrow, not more than $10 - 20 \text{ MeV}$, and centered around $T \approx 200 \text{ MeV}$. We will refer to this temperature in the following as T_c , but stress that, despite the curiously good agreement with the crossover temperature suggested by the lattice

¹We have corrected a minor error in the numerical results of ref. [43].

study mentioned [49], T_c does not need to coincide with any specific definition of T_c , given the inherent ambiguity in the location of a crossover. The significant benefit of this recipe, compared with lattice simulations, is that the results can be evaluated also at arbitrarily low and high temperatures without problems.

Now, this recipe is naturally not exact in the intermediate temperature range; the results can be improved when future lattice simulations get closer to the infinite-volume, continuum, and chiral limits. In order to estimate the uncertainties in the present implementation, we have considered two types of variations of the basic setup:

The shape and "sharpness" of the crossover can be changed by adding artificially heavy hadronic resonances to the gas, or removing existing ones.

The overall location of the pseudocritical temperature can be changed most simply by just rescaling the temperature units by some percentage amount.

It is naturally not difficult to come up with other possible variations as well, but as such recipes are purely phenomenological in any case, it is sufficient for our purposes to restrict to these most straightforward possibilities.

We find that the first of these variations has a relatively minor impact on the results. On the contrary, a change in T_c would lead to visible changes. Qualitatively, a low T_c implies a low abundance, since the results are inversely proportional to $g_e^{1=2} h_e$ (cf. Eq. (4.8)), and the production then peaks on the partonic side where $g_e^{1=2} h_e$ is higher. Consequently, we will assume in the following that the uncertainties of the equation-of-state can be sufficiently estimated by a rescaling of T_c by 20% in both directions, $T_c = (160 \text{--} 240) \text{ MeV}$, which should be a conservative estimate.

5.2. Vector and axial current spectral functions

As has been discussed in ref. [21], the hadronic contributions to $\text{Im } \Pi$ can be expressed through the spectral functions related to vector and axial currents with various flavours. The current status of the in general very demanding challenge of reliably determining these quantities was also reviewed in ref. [21].

Irrespective of all details, however, the general pattern we expect for the hadronic effects should be clear: at high temperatures $T \gg T_c$, hadrons should be reasonably represented by free quarks (cf. Eq. (3.3)), whereas once the temperature is lowered, confinement sets in, and all hadronic effects eventually switch on, given that all mesons and baryons are massive. For $T \ll T_c$, for instance, the hadronic spectral functions can be determined with chiral perturbation theory. It is easy to see that to leading order in the chiral expansion and assuming a mass-degenerate limit, only the flavour non-singlet axial current, denoted by A^a in ref. [21], contributes. We have verified explicitly that this dominant pionic contribution is strongly suppressed with respect to the leptonic contributions at all relevant temperatures (below 1%), for the small masses M_1 that we are interested in.

To give another argument in the same direction, we may reasonably assume that the hadronic effects are proportional to the number of effective hadronic degrees of freedom, h_e^{QCD} , related to the hadronic contribution to the entropy, which also rapidly decreases with the temperature (cf. Fig. 2).

These considerations suggest that a strict upper bound for the hadronic contribution to Im can be obtained by simply computing the effect of free quarks, Eq. (3.3). We take into account the u,d,s and c quarks, cf. Table 1, with their $\overline{\text{MS}}$ schemes [51]. A strict lower bound can obviously be obtained by simply setting $N_c = 0$ in the hadronic contributions listed in Table 1. As we have already mentioned, the "error bars" that result from this (clearly most conservative) procedure are roughly of the same order as those related to the equation-of-state, as defined in Sec. 5.1. (In fact they are a bit larger as we will see, but the recipe is also overly conservative.) Furthermore we define a phenomenological "mean" value by making use of the perturbative contribution in Table 1, but rescaling N_c by the factor $h_e^{QCD}(T)=58$, where 58 counts the hadronic degrees of freedom in the non-interacting four-flavour limit.

6. Numerical results for the sterile neutrino abundance

For the numerical evaluation of the sterile neutrino abundance it is useful to note that the computationally most demanding part entering our equations, Im , is practically independent of M_1 in the range $M_1 \gg T$ that we are interested in. Therefore, Im can be evaluated once and for all by using any fixed M_1 . In contrast, the "prefactor" (i.e. the parts of Eq. (2.8) other than Im) does depend strongly on the precise value of M_1 , yielding a non-trivial dependence on M_1 for the function $C(M_1)$ of Eq. (4.10).

As another comment, we note that for $q^0 > 0$ there are seven channels in Eq. (3.9) that can be realised. It can be verified numerically, however, that in practice only the 2×2 processes give a significant contribution; the other cases have a restricted phase space and amount to at most 5% of the 2×2 channels (for typical parameter values in fact much less than 5%), which is smaller than our uncertainties. To decrease the numerical cost, we have therefore omitted these contributions in the following. It may be noted, though, that these additional channels systematically increase the sterile neutrino abundance.

The way we have numerically evaluated the phase space integrations entering Im at the 2-loop level is explained in some detail in Appendix B. Once an efficient implementation is available, the remaining integrations (over T, q ; cf. Eq. (4.8)) are relatively straightforward. We note that the q -integration converges exponentially fast, and can in practice be limited to values $q=T < 10 \text{ keV}$.

In Fig. 3 we show an example of the T_0 -evolution of the function $C(M_1)$, as defined by Eq. (4.10). We observe that most of the sterile neutrino abundance is indeed generated at temperatures of a few hundred MeV for M_1 in the keV range.

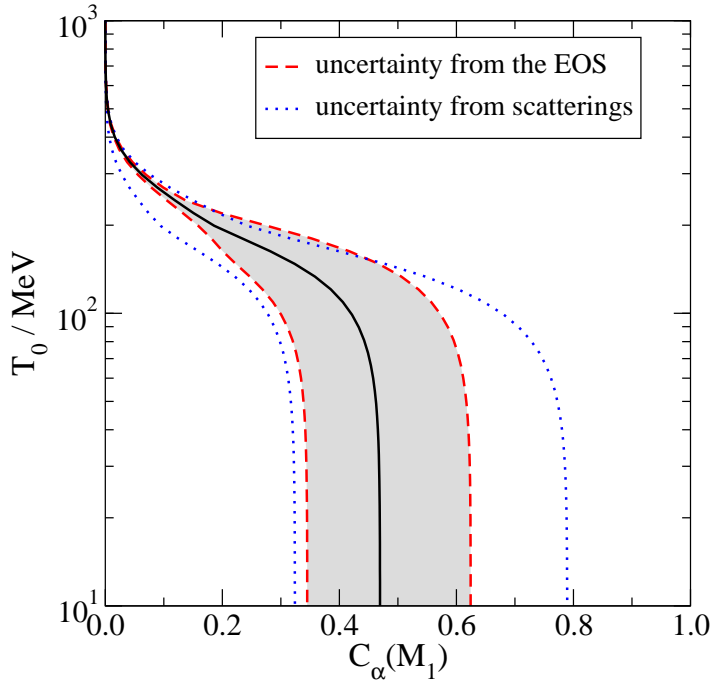


Figure 3: An example of the T_0 -evolution of C_α (cf. Eqs. (4.8)–(4.10)), for a fixed $\alpha = e$ and $M_1 = 10$ keV. Shown are the two sources of hadronic uncertainties that are discussed in the text: from the equation-of-state (EOS) and from hadronic scatterings.

In Fig. 4 the final low-temperature values of $C_\alpha(M_1)$ are shown as a function of α and M_1 . Importantly, we observe that the dependence on M_1 is fairly mild for a wide range of M_1 , say $M_1 = (0.1\text{--}10^3)$ keV, once expressed as in Eq. (4.10). This means, roughly speaking, that the relic density of N_1 is determined by the Dirac neutrino masses $M_D j_1$. According to Eq. (4.12) the Dirac neutrino masses should typically be $M_D j_1 \lesssim 0.1$ eV.

Furthermore, due to the differences between C_α , the relic abundance of N_1 depends on the flavour structure of the Dirac neutrino masses $M_D j_1$. We find the (moderate) hierarchy $C_e > C_\mu > C_\tau$. Thus, the largest abundance is obtained when

$$M_D j_1 \neq 0; \quad M_D j_1 = M_D j_1 = 0; \quad (6.1)$$

In this case (which we call ‘case 1’), we obtain the most stringent upper bound on θ^2 from Eq. (4.12). On the other hand, the case (which we call ‘case 2’) when

$$M_D j_1 \neq 0; \quad M_D j_1 = M_D j_1 = 0; \quad (6.2)$$

gives the smallest relic abundance and the weakest upper bound on θ^2 .

In Fig. 5, we show the upper bounds on the mixing angle for the above two cases. We also compare with the most recent previous computation from the literature [13]. It can be seen

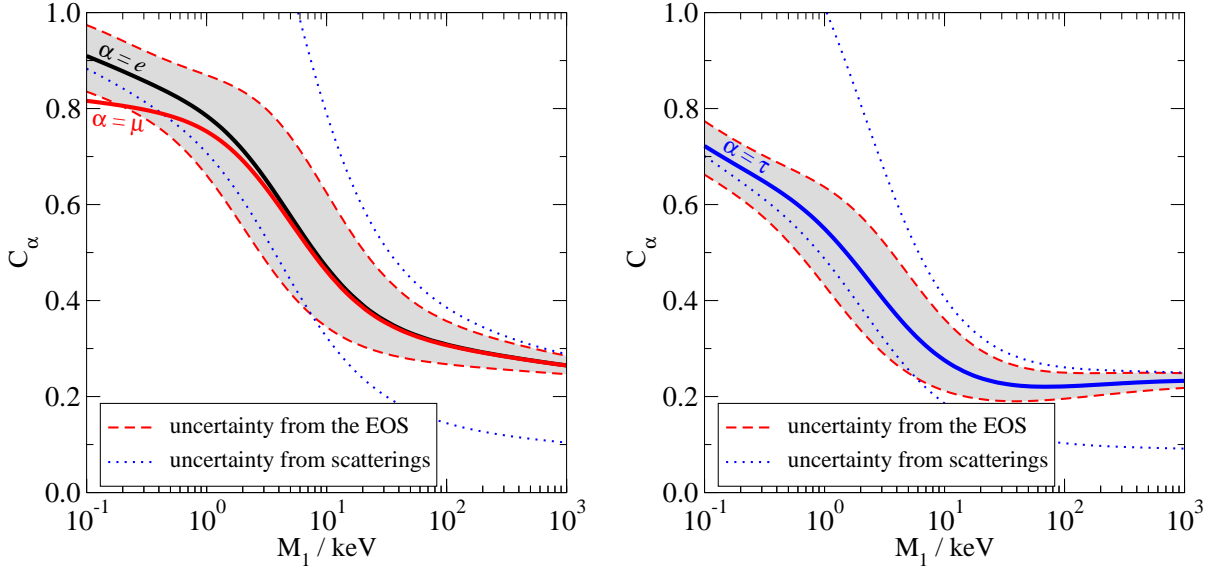


Figure 4: The functions $C(\mathcal{M}_1)$, together with estimated hadronic uncertainties, as described in the text (see also Fig. 3). Left: $\alpha = e$; , and only the uncertainties for $\alpha = e$ are shown. Right: $\alpha = \mu$.

that the bound obtained is rather insensitive to the flavour structure of the Dirac neutrino masses $\mathcal{M}_D j_1$, at least when plotted on a logarithmic scale.

If we ignore the dependence of C on \mathcal{M}_1 and α in Fig. 4, setting $C' = 0.5$, we obtain a very simple but useful approximate bound,

$$\sin^2(2\alpha) \cdot 4^{\frac{X}{2}} \cdot \mathcal{M}_1^2 < 8 \cdot 10^{-8} \cdot \frac{\mathcal{M}_1^2}{\text{keV}} : \quad (6.3)$$

More precise expressions, based on fitting the numerical data, will be given in Eqs. (7.1) of the next section. In Fig. 5 the units on the y-axis have been so chosen that a direct comparison with the approximate formula in Eq. (6.3) is possible.

An alternative normalization of the sterile neutrino abundance is given in Eq. (4.7), and the corresponding results are plotted in Fig. 6. It is observed that the abundance generated is typically much below its equilibrium value, as expected [recall that in order to avoid overclosure, $(\mathcal{M}_D j_1 = 0.1 \text{ eV})^2 < \text{a few}$, cf. Eq. (4.12) and Fig. 4].

Finally, in Fig. 7 we show the momentum distribution, $n_1(T; q)$, for a few examples, normalized to the massless equilibrium case, $n_{\text{eq}}(t_0; q) = 2n_F(q) = (2\pi)^3$. As noted in the literature [13], the momentum distribution is shifted towards the infrared compared with the equilibrium distribution. For heavy \mathcal{M}_1 the shift is fairly substantial (note the logarithmic scale). Structure formation simulations necessitate the momentum distribution function of dark matter as input, and curves such as the ones in Fig. 7 could be used for this purpose. However, as mentioned in Sec. 1, one may get a rough first impression of the results already by just rescaling the average momentum to a shifted value. To allow for such an estimate,

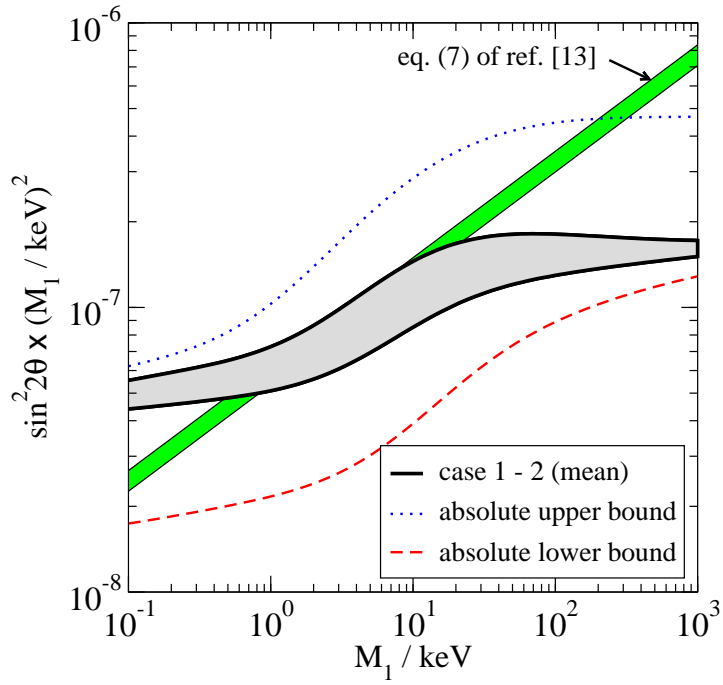


Figure 5: The parameter values that, according to our theoretical computation (cf. Fig. 4 and Eq. (4.10)), lead to the correct dark matter abundance in the Dodelson-Widrow scenario; if additional sources are present, $\sin^2 2\theta$ must lie below the curves shown. The grey region between case 1 (lower solid line) and case 2 (upper solid line) corresponds to different patterns of the active-sterile mixing angles, cf. Eqs. (6.1), (6.2). The absolute upper and lower bounds correspond to one of these mixing patterns with simultaneously the uncertainties from the EOS and from hadronic scatterings set to their maximal values. The yellow band indicates the result in Eq. (7) of ref. [13],² where we have inserted $\alpha_m = 0.20$, and varied the parameter T_c in the range $T_c = (150::200)$ MeV.

Fig. 8 displays the average momentum of the sterile neutrinos generated, in comparison with the equilibrium value for active neutrinos.

7. The Dodelson-Widrow scenario

We are now in the position to discuss the Dodelson-Widrow (DW) scenario for sterile neutrino dark matter, which is based on the assumptions (i)-(iv) we stated in Sec. 1. In this scenario, the initial abundance of the dark matter sterile neutrinos was zero at $T = 1$ GeV, and they were only produced in active-sterile neutrino transitions from the thermal plasma. Thus, in terms of Eq. (1.1), it is the maximal value of the mixing angle which realizes this scenario,

²Ref. [13] does not state explicitly the sterile neutrino mass range in which its Eq. (7) should be valid. After the eprint version of our paper had appeared, we were informed by K. Abazajian that Eq. (7) of ref. [13] was meant to be valid for 0.5 keV $< M_1 < 10$ keV.

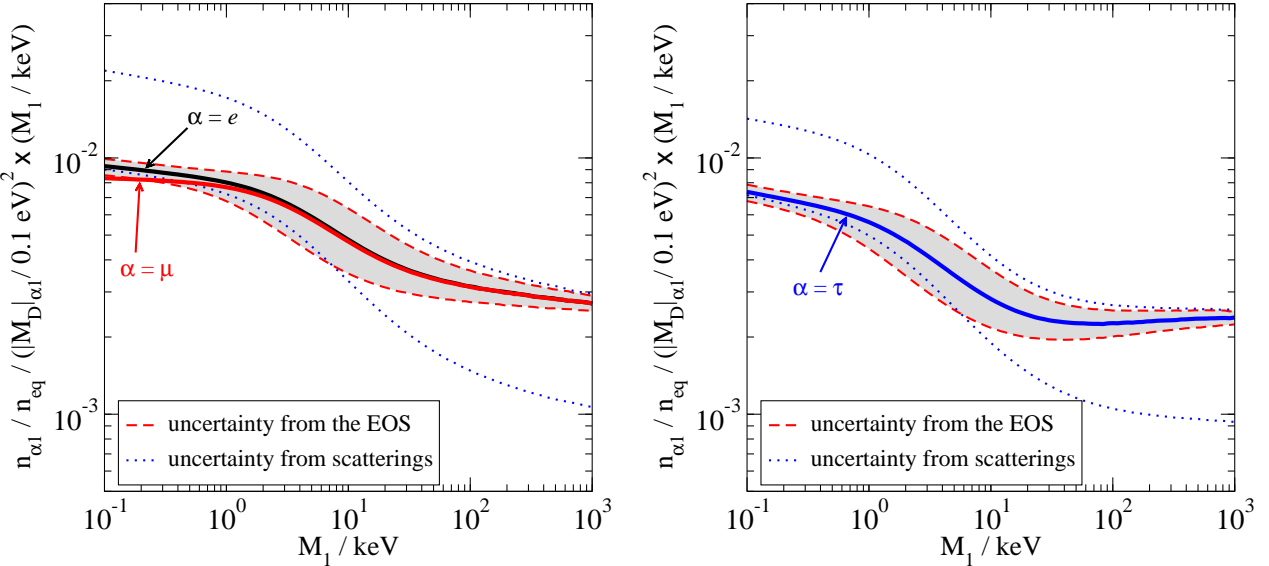


Figure 6: The sterile neutrino abundance ratio to its equilibrium abundance, $n_1 = n_{eq}$, at $T_0 = 1 \text{ MeV}$. Hadronic uncertainties have the same meaning as in Fig. 3. The combination $(M_D|_{j_1=0.1 \text{ eV}})^2$ has been factored out in analogy with Eq. (4.10) and, for better visibility, the results have been multiplied by $M_1 = \text{keV}$. Left: $\alpha = e$, and only the uncertainties for $\alpha = e$ are shown. Right: $\alpha = \tau$.

$\sin^2(2\theta) = f(M_1)$. We denote $M_s = M_1$ in this case. This scenario can be confronted with a number of cosmological and astrophysical observations.

In order to carry out a comparison with the various X-ray constraints that exist, we replotted the curves of Fig. 5 in Fig. 9 (for a subrange of mass values), and compare with the regions excluded according to refs. [20], [26]. To facilitate numerical estimates, we also note that in this mass range (and on the resolution of the logarithmic scale), the theoretical curves can be roughly approximated by straight lines,

$$\begin{aligned}
 \log_{10} [\sin^2 2\theta] &= 6.9267 - 1.7350 \log_{10} M_s = \text{keV} & \text{(absolute upper bound)} \\
 \log_{10} [\sin^2 2\theta] &= 7.0862 - 1.8451 \log_{10} M_s = \text{keV} & \text{(case 2, mean)} \\
 \log_{10} [\sin^2 2\theta] &= 7.2491 - 1.8359 \log_{10} M_s = \text{keV} & \text{(case 1, mean)} \\
 \log_{10} [\sin^2 2\theta] &= 7.6195 - 1.7428 \log_{10} M_s = \text{keV} & \text{(absolute lower bound)}
 \end{aligned} \quad : \quad (7.1)$$

These fits improve on the first approximation in Eq. (6.3). The lower bound of the region excluded by X-ray constraints will be denoted by $f_X(M_s)$; for this data a straight line is a worse approximation, but restricting to the mass range $M_s = (2::10) \text{ keV}$, the function can be roughly approximated by a parabola,

$$\log_{10} [\sin^2 2\theta] = 3.9499 - 9.7859 \log_{10} M_s = \text{keV} + 3.4902 \log_{10}^2 M_s = \text{keV} : \quad (7.2)$$

We then note that the intersection of $f(M_s)$ and $f_X(M_s)$ gives an upper bound on M_s . It is found from Eqs. (7.1), (7.2) that the bound $M_s < 3.5 \text{ keV}$ is obtained by using the mean

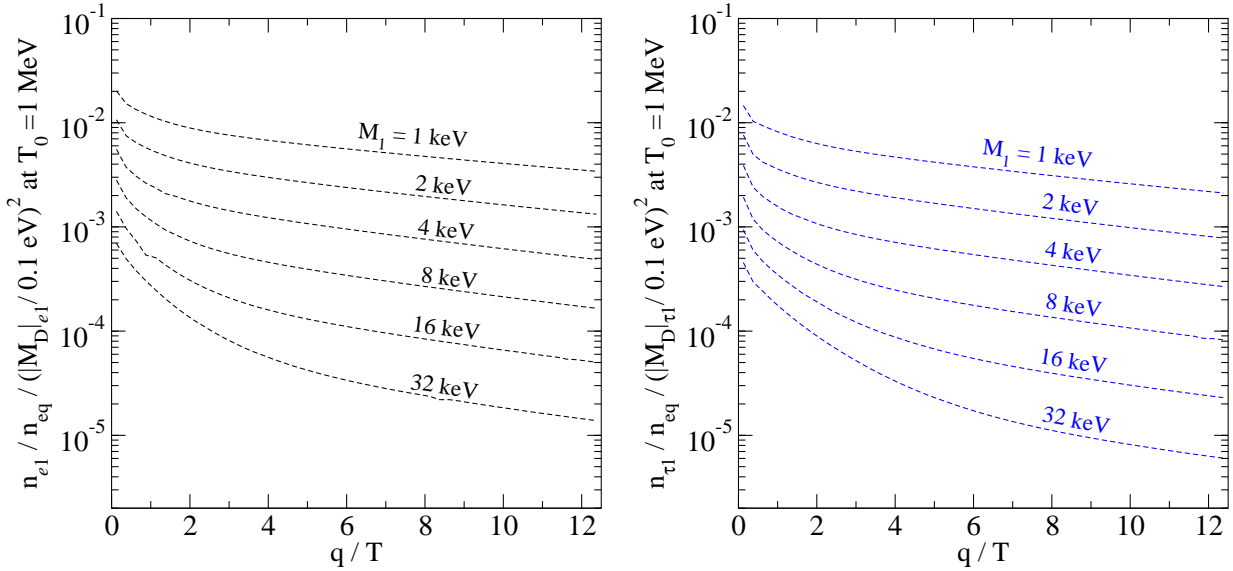


Figure 7: The distribution functions $n_1(t_0; q)$, for $T_0 = 1 \text{ MeV}$, normalized to the massless equilibrium case, $n_{\text{eq}}(t_0; q) = 2n_F(q) = (2\pi)^3$. The combination $(M_D j_1 = 0.1 \text{ eV})^2$ has been factored out in analogy with Eq. (4.10). Left: $= e$. Right: $= \tau$. These results can be compared with Fig. 1 of ref. [13], showing the same distribution functions for $0.3 \text{ keV} \leq M_1 \leq 140 \text{ keV}$; although similar at first sight, there are significant differences on closer inspection, for instance our curves are monotonic functions of q/T even for small M_1 , unlike those in ref. [13].

predictions for the cases 1 and 2 discussed in Eqs. (6.1), (6.2) of the previous section. For the most conservative case with respect to the hadronic uncertainties, the bound can be as large as $M_s < 4.3 \text{ keV}$. Adopting the absolute lower bound on $f(M_s)$ with the maximal hadronic uncertainties, and also assuming that the X-ray constraints are still uncertain by a factor of two, we set $M_s < 6 \text{ keV}$ as the most conservative limit. As we will show below, possible entropy dilution through the decays of the heavier sterile neutrino(s) makes this bound more severe, and, therefore, this bound is robust.

The fate of this scenario now depends on constraints from structure formation simulations, making use of Lyman- α observations, which give a lower bound on the mass of the dark matter sterile neutrino as $M_s > h_{j_s} j = h_{j_a} j M_0$, where $M_0 = 14.4 \text{ keV}$ (with $h_{j_s} j = h_{j_a} j' = 0.9$) [32] and $M_0 = 10 \text{ keV}$ (with $h_{j_s} j = h_{j_a} j' = 1.0$) [33] at 95% CL. Note, however, that these bounds are obtained by assuming that the sterile neutrino momentum distribution function is proportional to the Fermi-Dirac one (with a certain rescaling of the average momentum in ref. [32]), even though the sterile neutrino is not thermalized. As shown in Fig. 7, the momentum distribution function is in fact significantly distorted from the Fermi-Dirac shape towards the infrared (apart from having a smaller normalization). Assuming that the corresponding effects can be captured by the factor $h_{j_s} j = h_{j_a} j$, we read from Fig. 8 that $h_{j_s} j = h_{j_a} j' = 0.8$ for $M_s = 10 \text{ keV}$. Given that refs. [32, 33] assumed $h_{j_s} j = h_{j_a} j' = 0.9; 1.0$, respectively, the

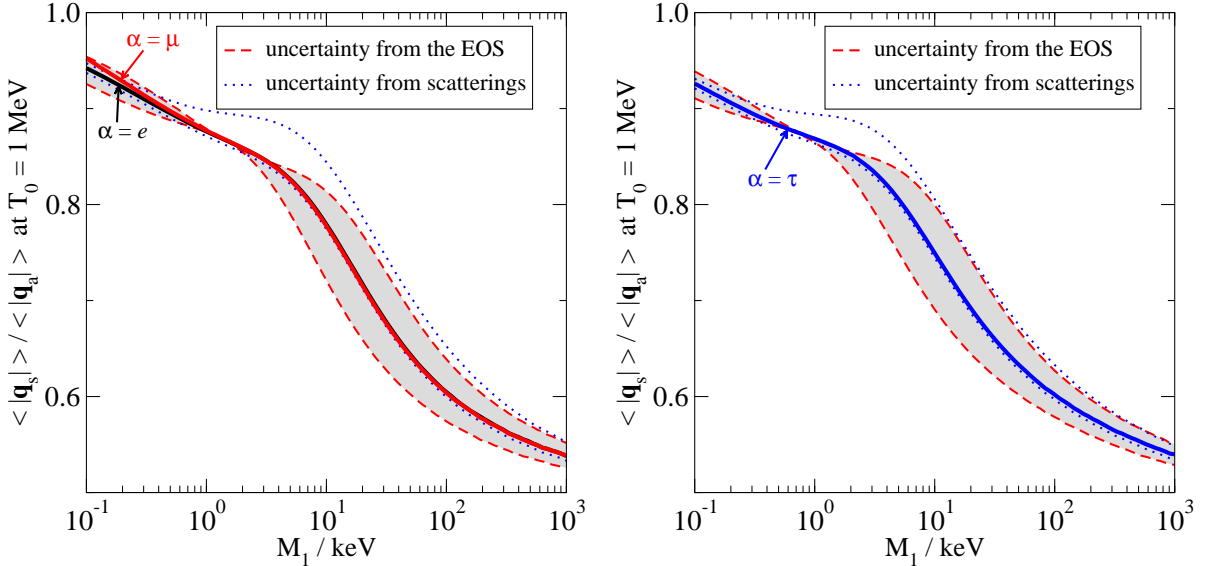


Figure 8: The average sterile neutrino momentum compared with the active neutrino equilibrium value, $h_{\bar{\nu}_s j}^j = h_{\bar{\nu}_a j}^j$, where $h_{\bar{\nu}_a j}^j = 7^4 T_0 = 180$ (3) $3:15 T_0$. Left: $\alpha = e$, and only the uncertainties for $\alpha = e$ are shown. Right: $\alpha = \tau$. We have assumed for this figure that only one of the mixing angles θ_1 is non-vanishing.

results for lower bounds can be re-interpreted as $M_s > 11.6 \text{ keV}$ and $M_s > 8 \text{ keV}$. Thus the X-ray and Lyman- α regions do not overlap, and astrophysical and cosmological constraints appear to rule out the DW scenario, in spite of all theoretical uncertainties involved in the computation. The scenario can only survive if the computations of refs. [32, 33] turn out to be uncertain for some reason, be it on the observational side, or on the theoretical side, related to the momentum distribution of the sterile neutrino (i.e., the need to use of the proper distribution function from Fig. 7 rather than the Fermi-Dirac one). We should mention that, even in such a situation, the Tremaine-Gunn lower bound $M_s > 0.3 \text{ keV}$ for fermionic dark matter does remain valid [36].

7.1. Entropy dilution

In the M SM, there are two heavier sterile neutrinos in addition to the lightest dark matter one. As shown in ref. [19], the heavier sterile neutrino(s) could completely dominate the energy density of the Universe, and their subsequent decay(s) could cause a significant entropy dilution after the dark matter sterile neutrinos have been produced. Here we briefly reiterate the corresponding effects, i.e., relax the assumption (iv) of Sec. 1.

Due to the entropy release, the yield Y_1 of the dark matter sterile neutrino is diluted by a factor S compared with that without the entropy dilution. Thus, the upper bound on the

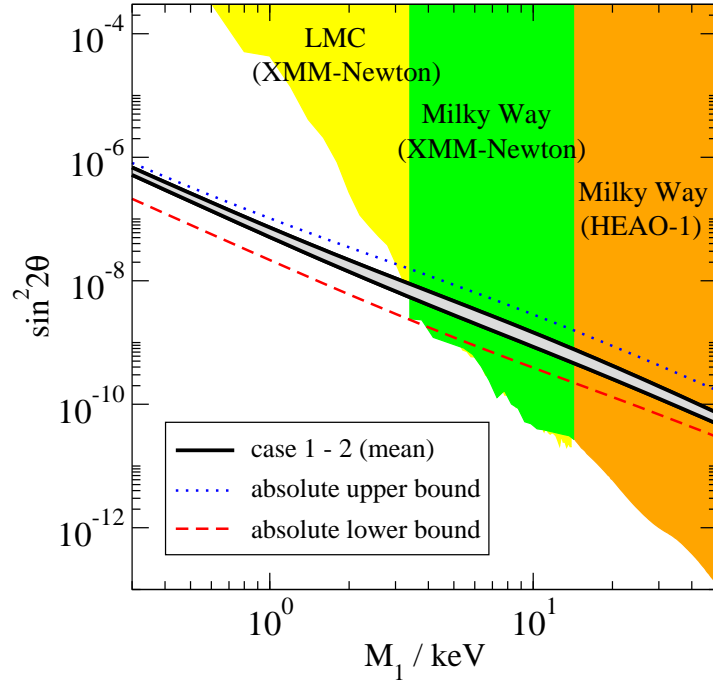


Figure 9: The central region of Fig. 5 ($M_1 = \text{keV} = 0.3 \dots 50.0$), compared with regions excluded by various X-ray constraints. From left to right, the X-ray constraints come from refs. [20], [26], [20], respectively. The abbreviation LMC stands for the Large Magellanic Cloud, and the names in the parentheses refer to the X-ray observatories whose data were employed for deriving the constraints.

active-sterile neutrino mixing angle becomes weaker,

$$\sin^2(2\theta) < f(M_s) \quad S : \quad (7.3)$$

Note that $f_X(M_s)$ from the X-ray constraints does not change, since f_X is derived from the present dark matter density ρ_{dm} . Then, we can see from Fig. 9 that the upper bound on M_s becomes more stringent for a larger S .

On the other hand, the lower bound on M_s from the Lyman- α observations also decreases if $S > 1$, by a factor $S^{1/3}$ if N_1 is out-of-equilibrium [19]. The combination of the two effects might open a window for sterile neutrino dark matter even in the presence of the Lyman- α constraints. To quantify the effect, we note that in the region $M_s < 4 \text{ keV}$, the X-ray bound can be approximated as $\log_{10}[\sin^2 2\theta] < 4.6121 - 6.4659 \log_{10} M_s \text{ keV}$; the most conservative bound from Eq. (7.1) becomes $\log_{10}[\sin^2 2\theta] < 7.6195 - 1.7428 \log_{10} M_s \text{ keV} + \log_{10} S$; and the Lyman- α bounds obtain the form $M_s < S^{1/3} > (8 \dots 11.6) \text{ keV}$.

If $M_s < S^{1/3} > 8 \text{ keV}$ from ref. [33], we find that there appears an allowed region for $S > 155$. When $S = 155$, a sterile neutrino with $M_s = 1.5 \text{ keV}$ and $\sin^2(2\theta) = 1.9 \times 10^6$ could function as dark matter and be consistent with X-ray and Lyman- α constraints. On the other hand, if $M_s < S^{1/3} > 11.6 \text{ keV}$ from ref. [32], there is an allowed region for $S > 3.3 \times 10^3$,

corresponding to $M_s < 0.78$ keV and $\sin^2(2\beta) > 1.2 \times 10^{-4}$. However, the combination $(M_D j_1 = 0.1 \text{ eV})^2 = 2.5 \times 10^7 (M_s \text{ keV})^2 \sin^2(2\beta)$ is larger than 10^3 in this case and, according to Fig. 6, N_1 are thermalized, whereby the assumptions we have made are no longer self-consistent. We discuss the correct procedure for the latter case in Sec. 7.2.

To sum up, we have learned that the Dodelson-Widrow scenario remains a possibility if there exists a large enough entropy dilution and if the lower bound on M_s from the Lyman-alpha data is small enough. However, it is very difficult to get such a large dilution factor within the M SM. It has been shown in ref. [19] that the M SM induces $S > 30$ at most and $S > 100$ is obtained only if there exists some physics beyond the M SM. Therefore, to realize this scenario, the constraints from the Lyman-alpha data should again be weaker than those presented in refs. [32, 33].

7.2. The case of thermalized sterile neutrinos

So far, we have assumed that the Dirac neutrino masses $M_D j_1$ are sufficiently small so that N_1 was never in thermal equilibrium. Now, let us discuss the possibility of thermalized N_1 as dark matter. If N_1 is thermalized at some high temperatures and decouples at $T = T_{d1}$, the present relic density is given by

$$N_1 h^2 = 10.6 \frac{M_s}{\text{keV}} \frac{10.75}{h_e(T_{d1})} : \quad (7.4)$$

Note that this result is independent of M_s as long as M_s is sufficiently large such that N_1 was thermalized at $T > T_{d1}$. To explain all of dark matter by such a density of N_1 's, the sterile neutrino mass should be

$$M_s' \text{ (10 eV)} \frac{h_e(T_{d1})}{10.75} : \quad (7.5)$$

The ratio $h_e = 10.75$ is at least unity, cf. Fig. 2. In any case, this value is much smaller than the Tremaine-Gunn bound, $M_s > 0.3$ keV, and is also below the bounds from the Lyman-alpha constraints for the thermalized case; $M_s > 2.4$ keV [32] and $M_s > 2$ keV [33] (at 95% CL).

If there exists entropy dilution, the mass of the once-thermalized dark matter sterile neutrino becomes

$$M_s' \text{ (10 eV)} \frac{h_e(T_{d1})}{10.75} \quad S : \quad (7.6)$$

On the other hand, the Tremaine-Gunn bound and the Lyman-alpha constraint remain unchanged. This is because the distribution function of the sterile neutrino was the Fermi-Dirac one at $T = T_{d1}$ and it is just red-shifted to the present time. Although the Tremaine-Gunn bound can be satisfied with $S > 30$, larger factors $S > 240$ and 200 are required to avoid the Lyman-alpha bounds from refs. [32, 33], respectively. Therefore, the thermalized N_1 can be dark matter within the M SM only if there is the largest possible entropy dilution and if the lower bound on M_s is given by the Tremaine-Gunn bound, rather than the Lyman-alpha bounds.

7.3. Summary

We have shown in this section that if the lower bound on M_s from the Lyman- data is indeed as found in refs. [32, 33], then there is no parameter space left within the M SM to realize the scenario of sterile neutrinos serving as warm dark matter, respecting the 'crucial' assumptions (i)–(iii) of Sec. 1.

Of course, this does not mean that the sterile neutrino is excluded as a dark matter candidate, but that at least one of the assumptions would have to be relaxed for this to be the case. For instance, sterile neutrinos could be produced mainly in interactions beyond the M SM, as in ref. [5]. Another logical possibility is that the Universe had substantial leptonic asymmetries at small temperatures, leading to a resonant production of sterile neutrinos [8]. In any event, for $M_s > 35$ keV (6 keV if all hadronic uncertainties are pushed in one direction and the strongest X-ray bounds are relaxed by a factor of two) the active-sterile transitions from the thermal charge-symmetric plasma cannot produce cosmologically interesting amounts of sterile neutrino dark matter.

Finally, we should like to stress that, within the corner of the parameter space that defines the M SM, the bound on the mixing angle $\sin^2(2\beta) < f(M_s)$, i.e. Eq.(4.12), gives a prediction on the mass scale of the lightest active neutrino, m_1 , whose see-saw formula includes the lightest Majorana mass M_1 only [1]. By setting $C(M_1) = 0.5$, we find

$$m_1 < \frac{M_D \beta}{M_1} < 2 \times 10^5 \text{ eV} \quad \frac{\text{keV}}{M_1} \quad : \quad (7.7)$$

If N_1 is the dark matter particle, its mass should in any case be $M_1 > 0.3$ keV from the Tremaine-Gunn bound. Then, we get the weakest bound as $m_1 < 6.7 \times 10^5$ eV, which is much smaller than the neutrino mass scales observed in the atmospheric and solar neutrino experiments. Furthermore, the upper bound on m_1 becomes smaller for a larger M_1 . This clearly excludes the possibility that the three active neutrinos are nearly degenerate in mass, and indicates that one could find the absolute values of the heavier active neutrino masses from the results of neutrino oscillation experiments [1]. These conclusions remain valid even if there is entropy production as long as non-thermalized sterile neutrinos play the role of dark matter.

8. Conclusions

In this paper we have studied the production of sterile neutrinos in the M SM through active-sterile neutrino transitions from a thermal plasma, which does not contain any significant asymmetries related to lepton numbers. Though a first-principles formula for the production rate exists, which is valid to all orders in the strong coupling constant, its practical evaluation is subject to a number of uncertainties related to the strong interactions. The purpose of this

paper has been to present a *realistic mean*" evaluation of the hadronic contributions, and to estimate conservatively all the uncertainties that this mean result is subject to.

The most important result of this paper is encoded in the four lines shown in Fig. 9. They correspond to the case when there is no entropy production ($S = 1$) due to the decay of the heavier sterile neutrinos of the M SM. The area above the dotted line is certainly excluded: the amount of dark matter produced would lead to the overclosure of the Universe. The region below the dashed line is certainly allowed: the amount of sterile neutrinos produced due to active-sterile transitions is smaller than the amount of dark matter observed. Any point in the region between the two solid lines (corresponding to the *most reasonable* model for the hadronic contributions that we have been able to come up with) can lead to dark matter generation entirely due to active-sterile transitions. A maximal variation of the parameters of our hadronic model extends this region to the space between the dotted and dashed lines. In the case of entropy production with a factor $S > 1.0$, all these four lines simply move up by a factor S .

As Fig. 9 shows, active-sterile transitions can account for all of dark matter only if $M_1 < 3.5$ keV, if the *most reasonable* hadronic model is taken. The most conservative upper limit would correspond to $M_1 < 6$ keV, if all uncertainties are pushed in the same direction and also if the most stringent X-ray bounds are relaxed by a factor of two. Therefore, if the Lyman- α constraints from refs. [32, 33] are taken for granted, the production of sterile neutrinos due to active-sterile neutrino transitions happens to be too small to account for the observed abundance of dark matter. In other words, physics beyond the M SM is likely to be required to produce dark matter sterile neutrinos. Another option is to assume that the Universe contained relatively large lepton asymmetries [8]. We would like to stress, though, that (apart from the astrophysical uncertainties related to the Lyman- α data) the simulations mentioned have not utilised the correct non-equilibrium momentum distribution functions as given in Fig. 7, and may thus contain systematic uncertainties.

Acknowledgements

The work of T.A. was supported in part by the grants-in-aid from the Ministry of Education, Science, Sports, and Culture of Japan, Nos. 16081202, 17340062 and 18740122, and that of M.S. by the Swiss National Science Foundation.

Appendix A . Two-particle phase space integrals

We discuss in this appendix how the phase space integrals of Eq. (3.1) can be reduced to a one-dimensional integration in order to allow for a numerical evaluation.

Let P be a time-like four-vector, $P^2 > 0$. We can then define a Lorentz-boost, γ_P , which takes us to the rest-frame with respect to P : $[\gamma_P P]^i = 0$, $i = 1; 2; 3$. We denote $\hat{Q} = \gamma_P Q$, with the components $\hat{Q} = (q^0; \vec{q})$. To be explicit, this Lorentz-boost is given by

$$q^0 = [q^0 + e \cdot q]; \quad (A.1)$$

$$\hat{q} = q - e \cdot q e + [\gamma_P^0 e - q] e; \quad (A.2)$$

where

$$= \frac{\dot{p}_j}{p^0}; \quad = \frac{1}{1 - \frac{e^2}{p^0} \gamma_P^2}; \quad e = \frac{p}{\dot{p}_j}; \quad (A.3)$$

Denoting by $f[u; P_1; P_2; Q]$ a generic Lorentz-scalar, for instance

$$f[u; P_1; P_2; Q] = 2Q \cdot \bar{p}_1 n_B(u - \bar{p}_1) [1 - n_F(u - \bar{p}_1)]; \quad (A.4)$$

as would be relevant for the second term in Eq. (3.1), we then consider the integral

$$I = \int \frac{d^3 p_1}{(2\pi)^3 2E_1} \int \frac{d^3 p_2}{(2\pi)^3 2E_2} (2\pi)^4 \delta^{(4)}(P_2 - P_1 - Q) f[u; P_1; P_2; Q]; \quad (A.5)$$

where $Q = (q^0; \vec{q})$, $P_i = (\mathbf{E}_i; p_i)$ are on-shell four-vectors. Making use of the Lorentz-boost introduced above, we rewrite the integration in a frame where Q is at rest, $\hat{q} = 0$:

$$I = \int \frac{d^3 \hat{p}_1}{(2\pi)^3 2\hat{E}_1} \int \frac{d^3 \hat{p}_2}{(2\pi)^3 2\hat{E}_2} (2\pi)^4 \delta^{(3)}(\hat{p}_2 - \hat{p}_1) \cdot \hat{E}_2 \cdot \hat{E}_1 \cdot M_I f[\hat{u}; \hat{P}_1; \hat{P}_2; \hat{Q}] \Big|_{\hat{q}=0} : \quad (A.6)$$

The integral over \hat{p}_2 is now trivial:

$$I = \frac{1}{(2\pi)^2} \int_0^1 \frac{d^3 \hat{p}_1}{4 \frac{\hat{p}_1^2 + m_1^2}{x^2 + m_1^2} \frac{\hat{p}_1^2 + m_2^2}{x^2 + m_2^2}} \frac{q}{(\hat{p}_1^2 + m_2^2)} \frac{q}{(\hat{p}_1^2 + m_1^2)} M_I \\ f[\hat{u}; (\hat{p}_1^2 + m_1^2; \hat{p}_1 \cdot \hat{p}_1); (\hat{p}_1^2 + m_2^2; \hat{p}_1 \cdot \hat{p}_1); \hat{Q}] : \quad (A.7)$$

Moreover the integral over \hat{p}_1 can be performed by making use of

$$\int_0^1 \frac{dx x^2 g(x)}{x^2 + m_1^2 x^2 + m_2^2} \frac{q}{(x^2 + m_2^2)} \frac{q}{(x^2 + m_1^2)} M_I = (m_2 - m_1 - M) \frac{\int_0^1 \frac{M}{x^2 + m_1^2} g(\frac{12M}{x^2 + m_1^2})}{M}; \quad (A.8)$$

where the function

$$g(M) = \frac{1}{2M} \frac{q}{M^4 - 2M^2(m_i^2 + m_j^2) + (m_i^2 - m_j^2)^2} \quad (A.9)$$

is real and positive for $0 < M < m_1 + m_2$ and $M > m_i + m_j$. The integral thus becomes

$$I = \frac{\frac{p_1 \cdot j}{(4\pi)^2 M_I}}{d_{p_1} f[u; (\hat{p}_1^2 + m_1^2; \hat{p}_1 \cdot j_{p_1}); (\hat{p}_1^2 + m_2^2; \hat{p}_1 \cdot j_{p_1}); (M_I; 0)]} : \frac{q}{\hat{p}_1 \cdot j_{12(M_I)}} \quad (A.10)$$

Now, the integrand in Eq. (A.10) depends on two spatial vectors, q , R_{p_1} , and thus on one angle. We can choose $q = (0; 0; \hat{q})$, $p_1 = (\sin \theta; 0; \cos \theta)$, $d_{p_1} = 2 \sin \theta d\theta d\sin \theta$. However, the Fermi distributions in Eq. (A.4) do depend on θ , because the spatial part of $q \cdot u$ is non-zero and proportional to q , so that the remaining integration is non-trivial. On the contrary, scalar products such as $Q \cdot P, Q \cdot \hat{P}, P_1 \cdot \hat{P}$ are independent of θ , because we can evaluate them in the "hatted" frame where $\hat{q} = 0$.

Appendix B. Three-particle phase space integrals

We discuss in this appendix how the phase space integrals of Eq. (3.9) can be reduced to a three-dimensional integration in order to allow for a numerical evaluation.

Denoting by $f[u; P_1; P_2; P_3; Q]$ a generic Lorentz-scalar, for instance

$$f[u; P_1; P_2; P_3; Q] = T_i n_F(u - P) n_F(u - \hat{P}) [1 - n_F(u - \hat{P})]; \quad (B.1)$$

where $T_i = T_1$ or T_2 from Eqs. (3.7) or (3.8), we consider the integral

$$I = \frac{\int d^3 p_1}{(2\pi)^3 2E_1} \frac{\int d^3 p_2}{(2\pi)^3 2E_2} \frac{\int d^3 p_3}{(2\pi)^3 2E_3} (2\pi)^4 \delta^{(4)}(P_1 + P_2 + P_3 - Q) f[u; P_1; P_2; P_3; Q]; \quad (B.2)$$

where $Q = (q^0; q)$, $P_i = (E_i; p_i)$ are on-shell four-vectors. Making use of the Lorentz-boost introduced in Appendix A, we rewrite a certain Lorentz-invariant subpart of the integration in a frame where $P_3 + Q$ is at rest, $\hat{p}_3 + \hat{q} = 0$:

$$I = \frac{\int d^3 p_3}{(2\pi)^3 2E_3} \frac{\int d^3 \hat{p}_1}{(2\pi)^3 2\hat{E}_1} \frac{\int d^3 \hat{p}_2}{(2\pi)^3 2\hat{E}_2} (2\pi)^4 \delta^{(3)}(\hat{p}_1 + \hat{p}_2) \hat{E}_1 + \hat{E}_2 + \hat{E}_3 - \hat{q}) f[\hat{u}; \hat{P}_1; \hat{P}_2; \hat{P}_3; \hat{Q}] \hat{V}_{P_3 + Q} : \quad (B.3)$$

The integral over \hat{p}_2 is now trivial:

$$I = \frac{\int d^3 p_3}{(2\pi)^3 2E_3} \frac{1}{(2\pi)^2} \frac{\int d^3 \hat{p}_1}{4 \frac{q}{\hat{p}_1^2 + m_1^2} \frac{q}{\hat{p}_1^2 + m_2^2}} \frac{q}{(\hat{p}_1^2 + m_1^2 + \hat{p}_1^2 + m_2^2) \hat{E}_3 - \hat{q}} f[P_3 + Q; (\hat{p}_1^2 + m_1^2; \hat{p}_1 \cdot j_{p_1}); (\hat{p}_1^2 + m_2^2; \hat{p}_1 \cdot j_{p_1}); P_3; Q] : \quad (B.4)$$

Moreover the integral over $\hat{p}_1 j$ can be performed by making use of

$$\int_0^{Z_1} \frac{dx x^2 g(x)}{q \frac{x^2 + m_1^2}{x^2 + m_2^2}} \left(\frac{q}{x^2 + m_1^2} + \frac{q}{x^2 + m_2^2} \right) \hat{E} = \hat{E} (m_1 m_2) \frac{\int_0^{12(\hat{E})} g(\hat{E})}{\hat{E}} ; \quad (B.5)$$

where the function g_{ij} is defined in Eq. (A.9). The integral thus becomes

$$I = \frac{Z}{(2\pi)^3 2E_3} \frac{1}{(4\pi)^2} \int_{\hat{p}_1}^Z \hat{E}_3 + \hat{q}^0 (m_1 m_2) \frac{\int_0^{12(\hat{E}_3 + \hat{q}^0)} g_{ij}}{\hat{E}_3 + \hat{q}^0} f_{[P_3+Q]} u; (\hat{p}_1^2 + m_1^2; \hat{p}_1 j_{\hat{p}_1}); (\hat{p}_1^2 + m_2^2; \hat{p}_1 j_{\hat{p}_1}); [P_3+Q] P_3; [P_3+Q] Q] ; \quad (B.6)$$

where $\hat{p}_1 j = \int_0^{12(\hat{E}_3 + \hat{q}^0)} g_{ij}$.

Now, the integrand in Eq. (B.6) depends on three spatial vectors, q, p_3, \hat{p}_1 , and thus in general on three angles. However, the Fermi distributions only depend on two angles, so that the dependence on the third angle is very simple and can be handled analytically. To implement this in practice we may for instance note that, due to $O(3)$ invariance, we can choose $q = (0; 0; \hat{p}_1 j)$ and p_3 in the $(x; z)$ -plane, $p_3 = \hat{p}_3 j(\sin \theta; 0; \cos \theta)$, so that

$$\int_{d^3 p_3}^Z \int_0^{Z_1} \int_0^Z \hat{p}_3 j d\hat{p}_3 j \sin \theta d\theta : \quad (B.7)$$

Defining the unit vector $e = (p_3 + q) = \hat{p}_3 + q j$ as before [it now lies within the $(x; z)$ -plane], we parametrize the remaining vector \hat{p}_1 by using spherical coordinates $(\hat{\theta}, \hat{\phi})$ with e as the polar axis. In the original frame, \hat{p}_1 is then given by $\hat{p}_1 = (e_z \sin \hat{\theta} \cos \hat{\phi}; e_x \cos \hat{\theta} \cos \hat{\phi}; e_z \sin \hat{\theta} \sin \hat{\phi}; e_x \cos \hat{\theta} \sin \hat{\phi})$. With this parametrization and given the form of f that appears in Eq. (B.1), it is not difficult to realize that the integrand depends on $\hat{\theta}$ only as a 2nd order polynomial in $\cos \hat{\theta}$: $f(\hat{\theta}) = a + b \cos \hat{\theta} + c \cos^2 \hat{\theta}$. Therefore we can replace

$$\int_0^{Z_2} d\hat{\theta} f(\hat{\theta}) = \frac{h}{f} \frac{1}{4} + f \frac{3}{4} \int_0^1 : \quad (B.8)$$

Only a three-dimensional integration (over $\hat{p}_3 j; \hat{\theta}, \hat{\phi}$) needs hence to be carried out.

Finally we remark that in the other channels ($3+1, 1+3$), the role of $P_3 + Q$ is played a difference, for instance $P_3 - Q$. For arbitrary $P_3; Q$ this is not necessarily time-like. However the δ -functions appearing in these channels always restrict the differences to be equal to a sum, for instance $P_1 + P_2$, which are time-like. Therefore non-zero contributions only emerge from regions of the phase space where $P_3 - Q$ is time-like, and the procedure described above can be taken over with minor modifications.

References

- [1] T. Asaka, S. Blandford and M. Shaposhnikov, Phys. Lett. B 631 (2005) 151 [[hep-ph/0503065](#)].
- [2] T. Asaka and M. Shaposhnikov, Phys. Lett. B 620 (2005) 17 [[hep-ph/0505013](#)]; M. Shaposhnikov, Nucl. Phys. B 763 (2007) 49 [[hep-ph/0605047](#)].
- [3] E.K. Akhmedov, V.A. Rubakov and A.Y. Smirnov, Phys. Rev. Lett. 81 (1998) 1359 [[hep-ph/9803255](#)].
- [4] V.A. Kuzmin, V.A. Rubakov and M.E. Shaposhnikov, Phys. Lett. B 155 (1985) 36.
- [5] M. Shaposhnikov and I. Tkachev, Phys. Lett. B 639 (2006) 414 [[hep-ph/0604236](#)].
- [6] A. Kusenko and G. Segre, Phys. Lett. B 396 (1997) 197 [[hep-ph/9701311](#)]; G.M. Fuller, A. Kusenko, I. Mocioiu and S. Pascoli, Phys. Rev. D 68 (2003) 103002 [[astro-ph/0307267](#)]; M. Barkovich, J.C. D'Olivo and R. Montemayor, Phys. Rev. D 70 (2004) 043005 [[hep-ph/0402259](#)]; M. M. Apelli, A. Ferrara and E. Pierpaoli, Mon. Not. Roy. Astron. Soc. 369 (2006) 1719 [[astro-ph/0603237](#)]; E. Ripamonti, M. M. Apelli and A. Ferrara, [astro-ph/0606482](#); E. Ripamonti, M. M. Apelli and A. Ferrara, [astro-ph/0606483](#); P.L. Biermann and A. Kusenko, Phys. Rev. Lett. 96 (2006) 091301 [[astro-ph/0601004](#)]; J. Stasiak, P.L. Biermann and A. Kusenko, [astro-ph/0606435](#); A. Kusenko, [hep-ph/0609081](#); F. Munyaneza and P.L. Biermann, [astro-ph/0609388](#); J. Hidaka and G.M. Fuller, [astro-ph/0609425](#).
- [7] S. Dodelson and L.M. Widrow, Phys. Rev. Lett. 72 (1994) 17 [[hep-ph/9303287](#)].
- [8] X. Shi and G.M. Fuller, Phys. Rev. Lett. 82 (1999) 2832 [[astro-ph/9810076](#)].
- [9] A.D. Dolgov and S.H. Hansen, Astropart. Phys. 16 (2002) 339 [[hep-ph/0009083](#)].
- [10] K. Abazajian, G.M. Fuller and M. Patel, Phys. Rev. D 64 (2001) 023501 [[astro-ph/0101524](#)].
- [11] K. Abazajian, G.M. Fuller and W.H. Tucker, Astrophys. J. 562 (2001) 593 [[astro-ph/0106002](#)].
- [12] K.N. Abazajian and G.M. Fuller, Phys. Rev. D 66 (2002) 023526 [[astro-ph/0204293](#)].
- [13] K. Abazajian, Phys. Rev. D 73 (2006) 063506 [[astro-ph/0511630](#)].
- [14] K. Abazajian and S.M. Koushiappas, Phys. Rev. D 74 (2006) 023527 [[astro-ph/0605271](#)].
- [15] D. Boyanovsky and C.M. Ho, [hep-ph/0612092](#).

[16] A.Boyarsky, A.Neronov, O.Ruchayskiy and M.Shaposhnikov, *Mon. Not. Roy. Astron. Soc.* 370 (2006) 213 [[astro-ph/0512509](#)].

[17] A.Boyarsky, A.Neronov, O.Ruchayskiy and M.Shaposhnikov, *JETP Lett.* 83 (2006) 133 [[hep-ph/0601098](#)].

[18] A.Boyarsky, A.Neronov, O.Ruchayskiy and M.Shaposhnikov, *Phys. Rev. D* 74 (2006) 103506 [[astro-ph/0603368](#)].

[19] T. Asaka, M. Shaposhnikov and A. Kusenko, *Phys. Lett. B* 638 (2006) 401 [[hep-ph/0602150](#)].

[20] A.Boyarsky, A.Neronov, O.Ruchayskiy, M.Shaposhnikov and I.Tkachev, *Phys. Rev. Lett.* 97 (2006) 261302 [[astro-ph/0603660](#)].

[21] T. Asaka, M. Laine and M. Shaposhnikov, *JHEP* 06 (2006) 053 [[hep-ph/0605209](#)].

[22] G.Gelman, S.Palmares-Ruiz and S.Pascoli, *Phys. Rev. Lett.* 93 (2004) 081302 [[astro-ph/0403323](#)].

[23] S.Riemer-Sorensen, S.H.Hansen and K.Pedersen, *Astrophys. J.* 644 (2006) L33 [[astro-ph/0603661](#)].

[24] C.R.Watson, J.F.Beaumon, H.Yuksel and T.P.Walker, *Phys. Rev. D* 74 (2006) 033009 [[astro-ph/0605424](#)].

[25] A.Boyarsky, O.Ruchayskiy and M.Markevitch, [astro-ph/0611168](#).

[26] A.Boyarsky, J.Nevalainen and O.Ruchayskiy, [astro-ph/0610961](#).

[27] S.Riemer-Sorensen, K.Pedersen, S.H.Hansen and H.Dahle, [astro-ph/0610034](#).

[28] K.N.Abazaian, M.Markevitch, S.M.Koushiappas and R.C.Hickox, [astro-ph/0611144](#).

[29] A.Boyarsky, J.W.den Herder, A.Neronov and O.Ruchayskiy, [astro-ph/0612219](#).

[30] S.H.Hansen, J.Lesgourgues, S.Pastor and J.Silk, *Mon. Not. Roy. Astron. Soc.* 333 (2002) 544 [[astro-ph/0106108](#)].

[31] M.Viel, J.Lesgourgues, M.G.Hahnelt, S.Matarrese and A.Riotto, *Phys. Rev. D* 71 (2005) 063534 [[astro-ph/0501562](#)].

[32] U.Seljak, A.Makarov, P.MDonald and H.Trac, *Phys. Rev. Lett.* 97 (2006) 191303 [[astro-ph/0602430](#)].

[33] M.Viel, J.Lesgourgues, M.G.Hahnelt, S.Matarrese and A.Riotto, *Phys. Rev. Lett.* 97 (2006) 071301 [[astro-ph/0605706](#)].

[34] S. Tremaine and J.E. Gunn, *Phys. Rev. Lett.* **42** (1979) 407.

[35] D.N.C. Lin and S.M. Faber, *Astrophys. J.* **266** (1983) L21.

[36] J.J. Dalcanton and C.J. Hogan, *Astrophys. J.* **561** (2001) 35 [[astro-ph/0004381](#)].

[37] F. Bezrukov and M. Shaposhnikov, [hep-ph/0611352](#).

[38] D. Notzold and G. Ratz, *Nucl. Phys. B* **307** (1988) 924; K. Enqvist, K. Kainulainen and J.M. Salamäki, *Nucl. Phys. B* **349** (1991) 754; J.C. D'Olivo, J.F. Nieves and M. Torres, *Phys. Rev. D* **46** (1992) 1172.

[39] C. Quimbay and S. Vargas-Castrillon, *Nucl. Phys. B* **451** (1995) 265 [[hep-ph/9504410](#)].

[40] D.N. Spergel et al., [astro-ph/0603449](#).

[41] K. Kajantie, M. Laine, K. Rummukainen and Y. Schroder, *Phys. Rev. D* **67** (2003) 105008 [[hep-ph/0211321](#)].

[42] A. Hietanen, K. Kajantie, M. Laine, K. Rummukainen and Y. Schroder, *JHEP* **01** (2005) 013 [[hep-lat/0412008](#)]; F. Di Renzo, M. Laine, V. Muccio, Y. Schroder and C. Tornero, *JHEP* **07** (2006) 026 [[hep-ph/0605042](#)].

[43] M. Laine and Y. Schroder, *Phys. Rev. D* **73** (2006) 085009 [[hep-ph/0603048](#)].

[44] A. Ali Khan et al. [CP-PACS collaboration], *Phys. Rev. D* **64** (2001) 074510 [[hep-lat/0103028](#)].

[45] C. Bernard et al., [hep-lat/0611031](#).

[46] Y. Aoki, Z. Fodor, S.D. Katz and K.K. Szabo, *JHEP* **01** (2006) 089 [[hep-lat/0510084](#)].

[47] S. Ejiri, F. Karsch, E. Laermann and C. Schmidt, *Phys. Rev. D* **73** (2006) 054506 [[hep-lat/0512040](#)].

[48] P. de Forcrand and O. Philipsen, [hep-lat/0607017](#); Y. Aoki, G. Endrodi, Z. Fodor, S.D. Katz and K.K. Szabo, [hep-lat/0611014](#).

[49] M. Cheng et al., *Phys. Rev. D* **74** (2006) 054507 [[hep-lat/0608013](#)].

[50] Y. Aoki, Z. Fodor, S.D. Katz and K.K. Szabo, *Phys. Lett. B* **643** (2006) 46 [[hep-lat/0609068](#)].

[51] W.-M. Yao et al. [Particle Data Group], *J. Phys. G* **33** (2006) 1.